International Journal of Heat and Mass Transfer 140 (2019) 303–330

Contents lists available at ScienceDirect

International Journal of Heat and Mass Transfer

journal homepage: www.elsevier.com/locate/ijhmt

Experimental and analytical investigation of flow loop induced instabilities in micro-channel heat sinks

Seunghyun Lee [a], V.S. Devahdhanush [b], Issam Mudawar [b,*]

[a] Gwangju Institute of Science and Technology Two-Phase Flow and Thermal Engineering Laboratory, School of Mechanical Engineering, 123 Cheomdangwagi-ro, Buk-gu, Gwangju 61005, South Korea

[b] Purdue University Boiling and Two-Phase Flow Laboratory (PU-BTPFL), School of Mechanical Engineering, 585 Purdue Mall, West Lafayette, IN 47907, USA

ARTICLE INFO

Article history:
Received 17 January 2019
Received in revised form 30 April 2019
Accepted 24 May 2019
Available online 11 June 2019

Keywords:
Micro-channel
Flow boiling
Flow condensation
Two-phase instabilities

ABSTRACT

Two-phase flow instabilities, both static and dynamic, are commonplace in closed two-phase loops. For two-phase micro-channel heat sinks, past studies have reported different types of instability, including density wave oscillation (DWO), pressure drop oscillation (PDO), and parallel channel instability (PCI). In the present study, emphasis is placed on identifying and suppressing dominant instabilities for flow boiling of R134a in a micro-channel heat sink having 609.6-mm long and 203.2-mm wide base area, and containing 100 of 1×1 mm^2 channels. A dominant charge transition instability (CTI) is identified as causing appreciable oscillations in both mass velocity and pressure drop. Discussed is how PID control could be used to suppress CTI. But PCI was also prevalent within individual CTI oscillation cycles, taking the form of comparatively small amplitude, high frequency oscillations. It is shown CTI and PDO are fundamentally different in that ensuing fluctuations in mass velocity and pressure drop are synchronized for the former, but out of phase for the latter. Additionally, CTI occurs in the positive slope region of the heat sink's pressure drop versus mass velocity characteristics, while PDO occurs in the negative slope region. A detailed analytical model is also presented to predict onset of CTI. Overall, this study shows how loop instrumentation signals may be used in the model to both predict and suppress instability.

1. Introduction

1.1. Modern cooling trends

Design challenges resulting from rapid increases in heat dissipation rate from electronic and power devices have triggered unprecedented focus on development of high-power-density cooling schemes. And, with heat flux in certain devices beginning to exceed 10^3 W/cm^2 [1], options are now limited to two-phase cooling schemes, which, unlike their single-phase counterparts, can capitalize upon the coolant's latent and sensible heat rather than sensible heat alone. This allows two-phase systems to achieve very high heat transfer coefficients and maintain much lower device temperatures.

For over three decades, investigators at the Purdue University Boiling and Two-Phase Flow Laboratory (PU-BTPFL) and other researcher groups worldwide have developed a broad variety of two-phase cooling solutions, both passive (pump-free) and pump driven [2,3]. Passive schemes rely on either capillarity [4,5] (*e.g.*, heat pipes, capillary pumped loops, and loop heat pipe), or gravity [6] (*e.g.*, thermosyphons) to circulate coolant in a cooling vessel or loop. While passive systems require minimal or no power to maintain coolant circulation, low coolant speed limits these system to relatively low to medium heat flux situation. On the other hand, high heat flux applications rely on use of a pump (or compressor for refrigeration-based solutions) to achieve the high coolant speeds essential to achieving very high heat transfer coefficients. Examples of two-phase pumped loop systems include those employing falling film [7,8], channel flow [9–11], mini/micro-channel flow [12–14], jet-impingement [15,16], and spray [17–19]. Additionally, 'hybrid cooling' pumped loop solutions have been developed, which combine the attributes of two or more flow configurations to ameliorate cooling performance [20,21].

A primary motivation for the present study is thermal management aboard reduced gravity or microgravity space systems. To manage heat removal from avionics and crew, these systems rely on a thermal control system (TCS), tasked with acquiring and moving the heat to a condenser, where it is rejected by radiation to deep space. Unlike pumped two-phase systems in Earth gravity, because of limited power budget, space-based TCS must operate

* Corresponding author.
E-mail address: mudawar@ecn.purdue.edu (I. Mudawar).
URL: https://engineering.purdue.edu/BTPFL (I. Mudawar).

https://doi.org/10.1016/j.ijheatmasstransfer.2019.05.077
0017-9310/

Nomenclature

A	area
A_{base}	total base area of heat sink
A_D	area of diagonal plane of condenser
A_{fin}	area of fin surface of condenser's finned tube
$A_{mc,ch}$	total cross-sectional area of micro-channels
A_T	area of traverse plane of condenser
A_{unfin}	area of bare surface of condenser's finned tube
C	fluid charge (mass)
c_p	specific heat at constant pressure
C_v	valve flow coefficient
D_h	hydraulic diameter
D_i	inner diameter of condenser tube
D_o	outer diameter of condenser tube
f_{app}	apparent friction factor
Fr	Froude number
G	mass velocity
g	gravitational acceleration
h	enthalpy; heat transfer coefficient
$\bar{h}_{air}$	average heat transfer coefficient on airside of condenser's finned tube
H_{ch}	micro-channel height
h_{fg}	latent heat of vaporization
H_{res}	fluid level in reservoir
j	Colburn j factor, $Nu/(RePr^{1/3})$
j_g^*	dimensionless vapor superficial velocity
k	thermal conductivity
L	length
L_{ch}	micro-channel length
$\dot{m}$	mass flow rate
m_{fin}	fin parameter
n	number of condenser tubes in same row, $n = 22$
N_{ch}	number of micro-channels in heat sink
N_{fin}	number of condenser fins per unit length
N_{row}	number of condenser tube rows, $N_{row} = 2$
Nu	Nusselt number
$\overline{Nu}$	average Nusselt number on airside of condenser's finned tube
P	pressure
p_{fin}	fin pitch
Pr	Prandtl number
P_R	reduced pressure
Q	volumetric flow rate
q''	heat flux
q''_B	heat flux based on total base area of heat sink
q''_{cond}	heat flux along inner perimeter of condenser
q''_H	heat flux based on heated perimeter of condenser
R	thermal resistance
Re	Reynolds number
Re_{equiv}	equivalent Reynolds number for finned and unfinned outer surfaces of condenser tube
r_{equiv}	equivalent radius of condenser tube
r_i	inner radius of condenser tube
r_o	outside radius of condenser tube
S	slip ratio
S_D	diagonal tube pitch of condenser
s_{fin}	space between adjacent condenser tube fins
S_L	longitudinal tube pitch of condenser
St	Stanton number, $Nu/(RePr)$
S_T	traverse tube pitch of condenser
Su	Suratman number, Re^2/We
T	temperature
t	time; oscillation period
$t_{CTI,charge}$	time corresponding to onset of oscillation in loop charge (C_{loop})
$t_{CTI,o}$	time corresponding to onset of charge transition instability (CTI)
t_{fin}	fin thickness of condenser tube
t_{norm}	time corresponding to resumption of normal operating conditions
T_{sat}	saturation temperature
t_{sup}	time corresponding to suppression of temperature fluctuations
U	overall heat transfer coefficient
v	specific volume
$V_{cond\text{-}mc}$	flow volume of loop components separating condenser and micro-channel module
$V_{mc\text{-}cond}$	flow volume of loop components separating micro-channel module and condenser
$V_{plenum,in}$	volume of micro-channel module's inlet plenum
$V_{plenum,out}$	volume of micro-channel module's outlet plenum
W_{ch}	width of micro-channel
We	Weber number
We^*	modified Weber number
W_w	half-width of copper sidewall separating micro-channels
X	Lockhart-Martinelli parameter
x	vapor quality
x_e	thermodynamic equilibrium quality
X_D	half diagonal tube pitch of condenser
X_L	half longitudinal tube pitch of condenser
X_T	half traverse tube pitch of condenser
z	axial direction coordinate

Greek symbols

α	void fraction
η_{fin}	fin efficiency
μ	viscosity
ρ	density
ρ_H	two-phase mixture density based on Homogeneous Equilibrium Model
σ	surface tension
ϕ	fin parameter
ϕ^2	two-phase pressure drop multiplier

Subscripts

A	accelerational
air	airside
amb	ambient
c	contraction
cond	condenser
ch	channel
CTI	charge transition instability
e	expansion
equil	equilibrium condition
equiv	equivalent property
exp	experimental (measured)
F	frictional
f	liquid
fin	condenser tube fin
fo	liquid only
g	vapor
go	vapor only
in	inlet
k	*f* (liquid) or *g* (vapor)
ko	*f* (liquid) only or *g* (vapor) only
lam	laminar flow
loop	loop (without reservoir)
mc	micro-channel heat sink

min	minimum
o	onset of instability
out	outlet
pred	predicted
res	reservoir
sat	saturation
set	set condition; PID set value
sp	single phase
tc	thermocouple
tp	two phase
tt	turbulent liquid-turbulent vapor flow
turb	turbulent flow
unfin	bare surface of condenser's finned tube
w	condenser tube wall
z	axial direction coordinate

Acronyms

CHF	critical heat flux
CTI	charge transition instability
DWO	density-wave oscillation
PCI	parallel channel instability
PDO	pressure drop oscillation
TCS	thermal control system

with minimal pumping power, and do so in a very reliable manner. This task is complicated by appreciable variations in gravity during different stages of a space mission [22]. Through partnership with the NASA Glenn Research Center, PU-BTPFL investigators have conducted two decades of research centered on both flow boiling [23–26] and flow condensation [27] in reduced gravity. The present study is a continuation of these efforts.

1.2. Advantages and drawbacks of two-phase micro-channel heat sinks

Two-phase micro-channel heat sinks have recently emerged as one of the most effective thermal management solutions for high heat flux applications. Comprised of a thermally conducting substrate containing multiple parallel small hydraulic diameter channels with shared inlet and outlet plenums, they combine a number of both thermal and system attributes. These include high heat transfer coefficient, low temperature gradients, compact and lightweight packaging, as well as adaptability to different flow system configurations, including pumped loop [2], pumpless gravity-driven loop [14], and vapor compression [22].

In the earliest comprehensive study on two-phase flow and heat transfer characteristics of micro-channel heat sinks, Bowers and Mudawar (see [2]) showed that, despite these important attributes, micro-channel devices pose a number of challenges arising mostly from small hydraulic diameter and correspondingly high pressure drop (compared to single-phase micro-channel heat sinks). Most concerning among those are accentuated compressibility (pressure-gradient induced changes in specific volumes of vapor and liquid) and flashing (pressure-gradient induced changes in enthalpies of vapor and liquid). Combined with high mass velocity, strong compressibility and flashing increase likelihood of two-phase choking, especially as hydraulic diameter is greatly decreased. Another concern with micro-channel heat sinks is severe pressure drop causing vapor back flow and premature critical heat flux (CHF) [28].

This phenomenon is closely related to tendency of two-phase micro-channel heat sinks to trigger flow instabilities. These anomalies can be manifest in different forms, including mild pressure oscillation, severe pressure oscillation, density wave oscillation, and parallel channel instability; some of which overlap with others [29]. Investigators have pursued several strategies to combat these instabilities, most common of which is to throttle the flow upstream (also downstream) of the micro-channel heat sink in order to isolate the heat sink from loop compressibility effects [29–31]. But, while this might eliminate severe pressure oscillation, mild pressure oscillation has been reported to persist. Another strategy to tackle instabilities that lead to vapor backflow and premature CHF is to increase the heat sink's both mass velocity and inlet subcooling [28].

More recently, the authors of the present study performed extensive heat transfer measurements coupled with detailed high-speed video analysis of bubble nucleation and growth along a large length-to-diameter heat sink [32], same as one used in the present study. They encountered instabilities comprised of flow periodicity, which culminated in three distinct forms of dry-out: *intermittent*, *partial*, and *complete*. There were also appreciable temporal variations of flow pattern, from bubble all the way to annular, as well as local heat transfer fluctuating from nucleate boiling dominant to convective boiling, with the periodicity often associated with transient vapor back flow [33,34].

1.3. Instabilities in two-phase systems

Two-phase flow instabilities can be categorized into two main groups: *static* and *dynamics*. A system is considered statically unstable if, following a disturbance, it is unable to restore original operating conditions. The most well known manifestation of this phenomenon is the *Ledinegg instability*, which occurs when slope of internal characteristics curve of the boiling component of a two-phase loop is smaller than that of loop components external to the boiling component [35],

$$\left(\frac{\partial \Delta P}{\partial G}\right)_{int} \leqslant \left(\frac{\partial \Delta P}{\partial G}\right)_{ext}. \tag{1}$$

This type of instability has been observed to cause maldistribution in parallel flow systems [36], and might therefore precipitate serious flow boiling anomalies in a multi-channel heat sink. In fact, recent studies have shown increasing number of channels in the heat sink accentuates the flow maldistribution [37].

Dynamic instability is defined as any flow oscillations sustained by feedback among pressure drop, mass flow, and density changes. Two manifestations of dynamic instability are *density-wave oscillation* (DWO) and *pressure drop oscillation* (PDO). The former occurs in the positive slope region of the internal characteristics curve, Eq. (1), and the latter in the negative slope region, where slope of internal characteristics curve of the boiling component is greater than that of external loop components,

$$\left(\frac{\partial \Delta P}{\partial G}\right)_{int} > \left(\frac{\partial \Delta P}{\partial G}\right)_{ext}. \tag{2}$$

One reason for cyclical flow rate and density changes of DWO is delayed mass flow response to changes in pressure drop, which occur near the intersection of internal and external characteristics curves [38,39]. On the other hand, as indicated by Qu and Mudawar [29] for two-phase micro-channel heat sinks, PDO is associated with significant oscillations in both pressure drop and mass flow rate, and attributed to interaction of two-phase flow in the heat sink with upstream compressible volume, mostly in the loop's

reservoir. These oscillations occur in unison among parallel micro-channels, and could be effectively removed with the aid of a throttling valve situated upstream of the heat sink to isolate it from the upstream compressible volume. However, random, small amplitude oscillations in pressure drop and mass flow rate, commonly identified as *parallel channel instability* (PCI), could not be eliminated by the throttling valve. In general, PCI is influenced by DWO occurring in individual parallel channels sharing inlet and outlet plenums. Recent investigations have revealed important influences of PCI on thermal performance of two-phase heat sinks [33,40].

Recently, studies at PU-BTPFL provided more in-depth characterization of two-phase instabilities, including impact of PCI and ensuing periodic fluctuations of flow rate and pressure drop on thermal performance of two-phase micro-channel heat sinks employed in vapor compression systems [32,41,42] and pumped loops [33,34,43]. These studies also included impact of DWO on flow boiling in macro-channels [44], theoretical treatment of DWO [45], and role of gravity in instabilities in both flow boiling [46] and flow condensation [47].

These studies point to both the importance of understanding instability mechanisms and their impact on reliability of the entire two-phase cooling system.

1.4. Objectives of study

As discussed above, the present authors have recently provided significant insight into flow instabilities in a heat sink containing a large number of parallel, large length-to-diameter micro-channels. While some of these instabilities were relatively mild and persisted under normal system operation, others were abnormally severe, featuring both high amplitude and long oscillation period. Additionally, the more severe instability was found to be different from PDO. This distinction and importance of characterizing the impact of different forms of instability are key goals of the present study. More specifically, this study aims to achieve the following goals:

1. Identify trigger mechanisms for different types of instability for two-phase micro-channel heat sinks.
2. Explore parametric effects of heat flux, reservoir pressure, and ambient temperature on the trigger mechanisms.
3. Elucidating thermal performance changes in response to different forms of instability in regards to variations of dominant heat transfer characteristics as compared to those under stable conditions.
4. Explore details of pressure drop and mass velocity oscillations during instability, as well as both internal and external characteristics curves, and contrast dominant trends with those for PDO.
5. Investigate the role of measured fluctuations of coolant mass (charge) in the micro-channel heat sink, loop components (minus reservoir) external to the heat sink, and reservoir using a new analytical instability model.

2. Experimental methods

2.1. Two-phase flow loop and micro-channel module

Fig. 1(a) shows a schematic diagram of the two-phase loop used to achieve desired operating conditions at the inlet of a micro-channel test module using R134a as working fluid. The fluid is circulated in the loop with the aid of a magnetically-coupled Micropump GB series gear pump fitted with Baldor AC duty Microdrive controller to regulate flow rate. Subcooled liquid from the pump is passed through a Flow Technology FTO series turbine flow meter, followed by a control valve with $C_V = 1.8$. The latter is situated immediately upstream of the micro-channel test module, and serves to adjust both pressure and flow rate, and help prevent severe pressure drop oscillation. Within the test module, heat supplied from a Watlow thick-film resistive heater causes the fluid to change phase, from subcooled liquid to two-phase mixture or superheated vapor at the outlet. The fluid then passes through a Trenton TCS series air-cooled condenser, where it rejects heat to the ambient and returns to subcooled liquid state. System pressure is set downstream of the condenser at a junction connecting the loop to a reservoir that is fitted with both PID-controlled immersion heater and Lytron modular condensing unit. Downstream from this junction, the flow is subcooled further by passing through a SWEP plate-type heat exchanger, which rejects heat to the ambient using a second Lytron modular cooling unit, preventing any vapor bubbles from entering the gear pump. Fig. 2(b) provides images of both the micro-channel module and test facility.

The main component of the test module is a copper heat sink having a base heat transfer area 609.6-mm long and 203.2-mm wide, and featuring 100 of $1 \times 1\text{-mm}^2$ micro-channels those are machined into its top surface. The heat is supplied from the Watlow resistive heater, which is pressed against the heat sink underside. The large length to diameter of the micro-channels ($L_{ch}/D_h = 609.6$) is essential to the ability to perform experiments that could capture axial variations of both flow patterns and dominant heat transfer mechanisms. To minimize heat loss, the copper heat sink is mounted in a fiberglass plastic housing and fitted beneath with another fiberglass plastic insulating plate. The micro-channels are sealed atop with a transparent polycarbonate cover plate, which also provides optical access to the flow within. Given the large base area of the heat sink, the test module is fitted atop with a stainless steel brace plate and aluminum support bars and below with another set of aluminum bars. The main functions of this support are to prevent fluid leaks from the test module as well as close the gap between polycarbonate cover plate and micro-channel tops. Additional details of the test module's construction are available in [43].

2.2. Measurement instrumentation and data acquisition

Ten of grounded E-type thermocouples were inserted into the test module's copper heat sink at different axial locations, as indicated in Table 1, and one thermocouple in each of inlet and outlet plenums. Using a Neslab RTE-220 temperature-controlled thermal bath with 0.1 °C accuracy, all of the system's thermocouples (12 in test module and 6 in loop) are carefully calibrated over a range from −22.5 °C to 80 °C against a standard platinum resistance thermometer having an accuracy of ±0.03 °C. The calibration consists of bunching together tips of all thermocouples along with resistance thermometer in the thermal bath, and repeating steady-state measurements in 2.5 °C increments. The bath consists of distilled water for calibrations above 7.5 °C, and 50% volume ethylene glycol-water mixture for lower temperatures. Using 4th order polynomial curve fits, overall measurement accuracy of thermocouples following calibration is estimated at ±0.1 °C.

Two absolute and one differential Omega MM-series pressure transducers are installed across the inlet and outlet plenums of the micro-channel test module. Pressure transducers are also installed at the condenser's inlet and outlet, top of the reservoir, and upstream of the control valve. Volumetric flow rate is measured by a Flow technology FTO series turbine flow meter. Voltage, current, and power supply from the test module's thick film resistor are measured using a Yokogawa WT 310 m. A Gems XT-800 sensor is installed in the reservoir to measure liquid level with minimum resolution of 6.35 mm (equivalent to about 0.5 kg of R134a).

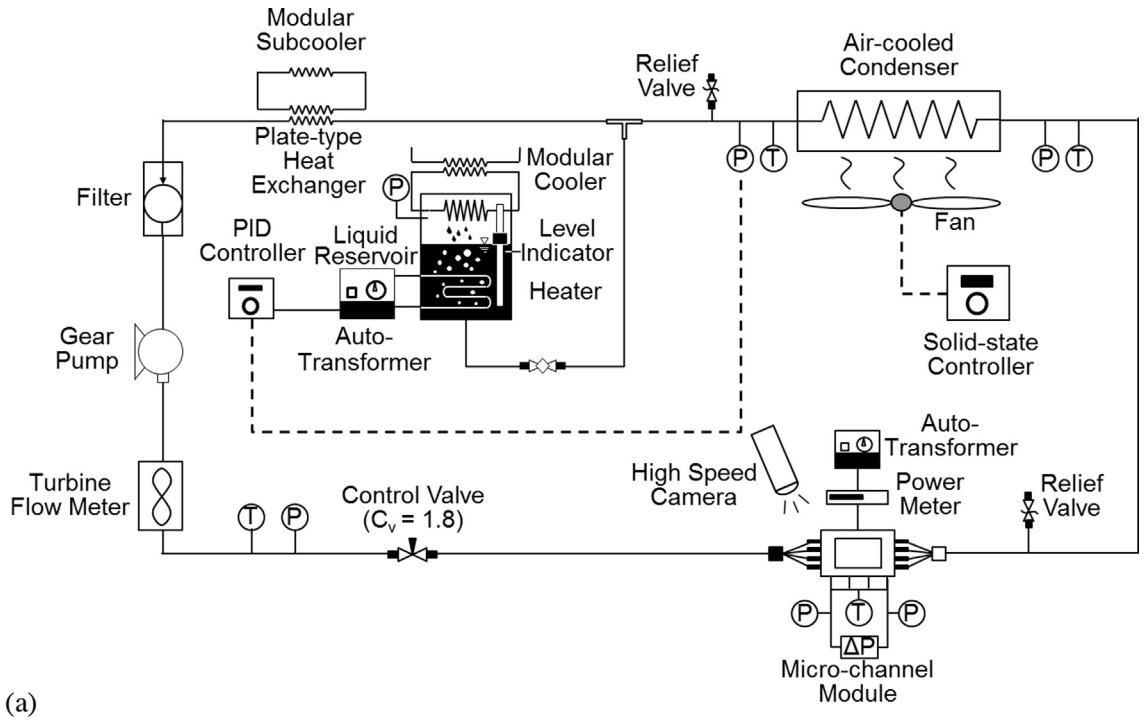

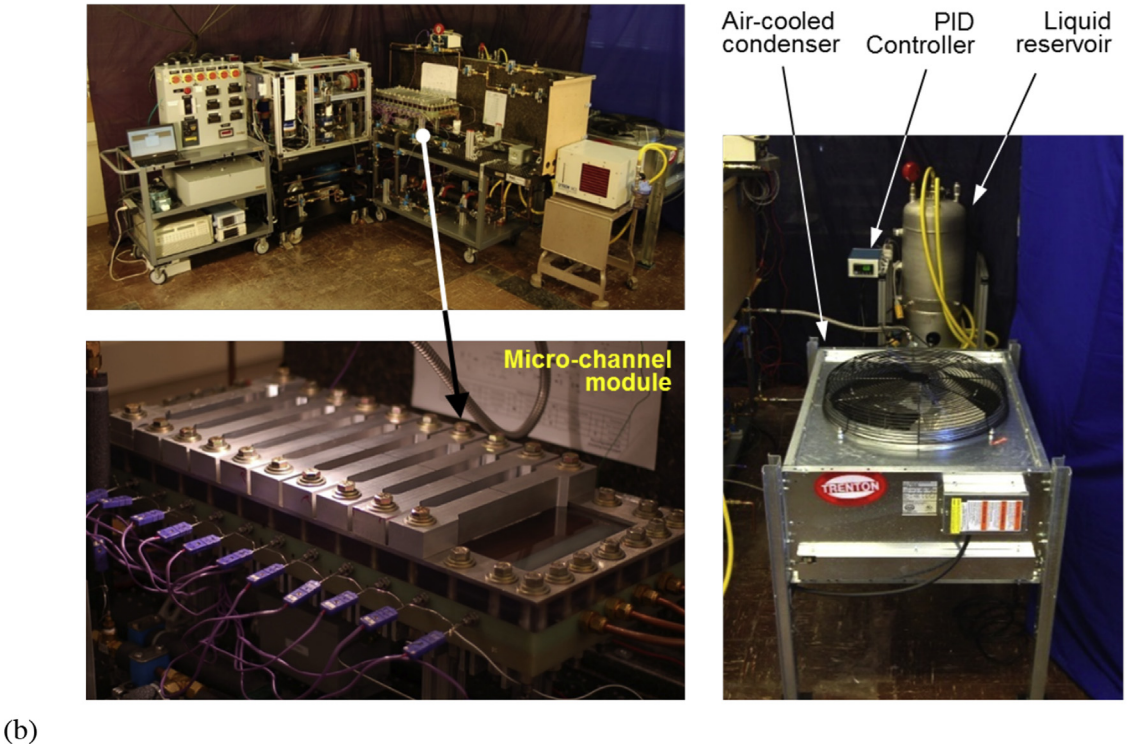

Fig. 1. (a) Schematic diagram of two-phase flow loop. (b) Photos of test facility.

An FET multiplexer is used to collect μV signals from thermocouples and 0–10 V analog signals from pressure transducers, flow meter, power meter, and liquid level indicator; these signals are by an HP voltmeter and processed using an HP data acquisition system. Both low and high frequency oscillations are captured from 1-kHz pressure transducers signals, and records of all other instrumentation signals are sampled at 2.5 Hz using a Labview code. Steady state data are processed separately at least one hour from experiment initiation.

As indicated in Table 2, maximum errors in measurements of absolute pressure, differential pressure, temperature, mass flow rate, heat input, and level indicator are ±0.1%, ±0.1%, ±0.1 °C,

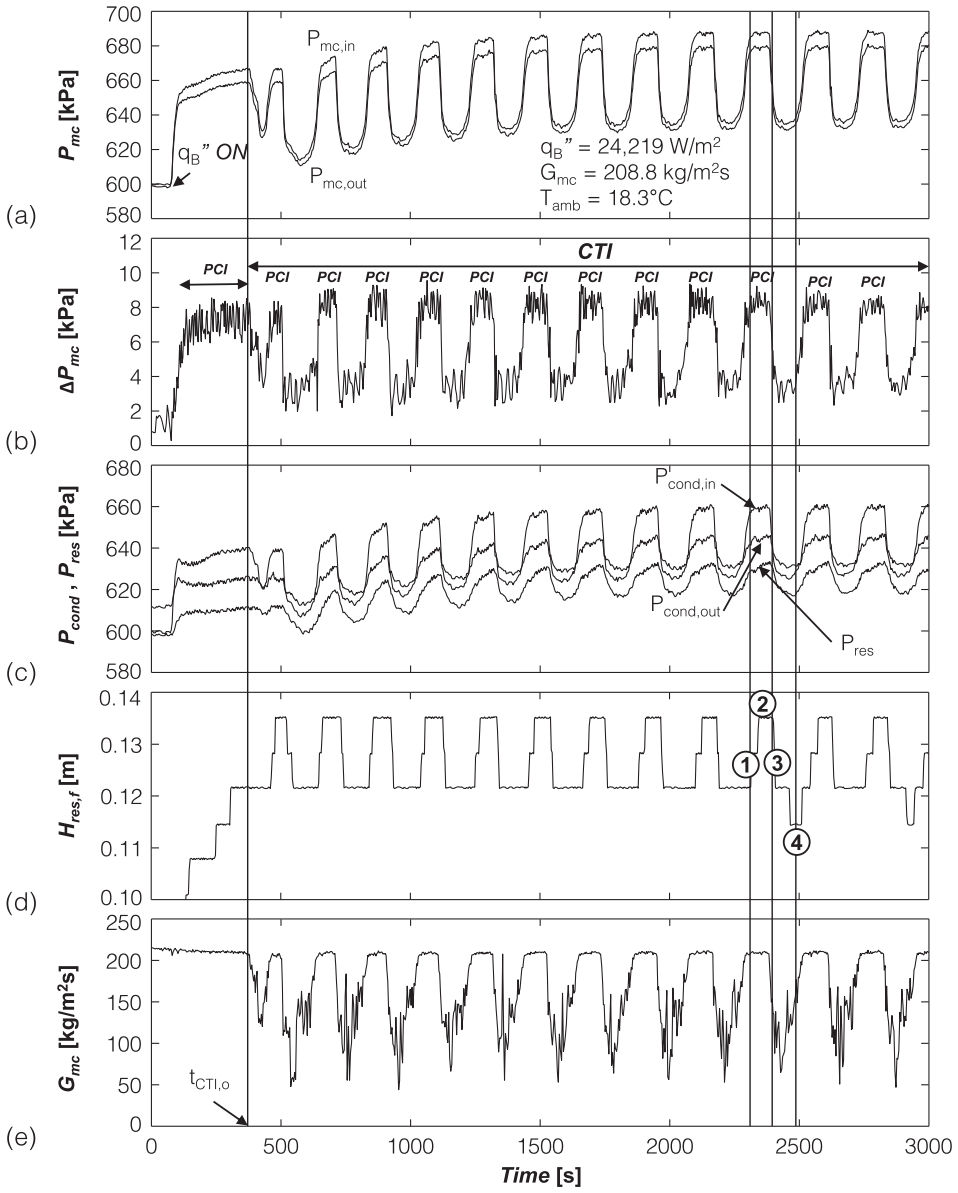

Fig. 2. Charge transition instability (CTI) without PID control and transient response at G_{mc} = 208.8 kg/m² s, T_{amb} = 18.3 °C, and q_B'' = 24,218.8 W/m² for (a) $P_{mc,in}$ and $P_{mc,out}$, (b) ΔP_{mc}, (c) $P_{cond,in}$, $P_{cond,out}$, and P_{res}, (d) $H_{res,f}$, and (e) G_{mc}.

Table 1
Micro-channel heat sink dimensions.

Length [mm]	Width [mm]	Number of channels	Axial locations of thermocouples [mm]
609.6	203.2	100	44.2, 102.1, 160.0, 217.9, 275.8, 333.8, 391.7, 434.3, 507.5, 565.4

Table 2
Measurement error and uncertainty propagation.

Parameter	Error	Parameter	Uncertainty
Absolute pressure	±0.1%	Heat transfer coefficient, h	≤5.92%
Differential pressure	±0.1%	Pressure drop, ΔP	≤0.1%
Temperature, T	±0.5%	Vapor quality change, Δx_e	≤3.23%
Mass flow rate, $\dot{m}$	±0.12%		
Heat input, Q	±0.3%		
Level indicator	6.35 mm		

±0.12%, ±0.3%, and 6.35 mm, respectively. Uncertainty propagation in calculating heat transfer coefficient, pressure drop, and vapor quality change are less than 13.46%, 0.1% and 0.16%, respectively.

2.3. Operating conditions

The test module's thermodynamic equilibrium inlet quality, $x_{e,in}$, is calculated using

$$x_{e,mc,in} = \frac{h_{mc,in} - h_f}{h_{fg}} = -\frac{c_{p,f}\left(T_{sat} - T_{mc,in}\right)}{h_{fg}} \quad , \tag{3}$$

where $c_{p,f}$, T_{sat} and h_{fg} are based on measured inlet pressure, $P_{mc,in}$, while inlet temperature, $T_{mc,in}$, is measured by the thermocouple in the inlet plenum. The test module's outlet quality, $x_{e,mc,out}$, is determined using

$$x_{e,mc,out} = x_{e,mc,in} + \left(q_B'' A_{base}\right)/\left(\dot{m}\, h_{fg}\right) , \tag{4}$$

Table 3
Operating conditions of micro-channel module.

G_{mc} [kg/m^2 s]	q_B" [W/m^2]	$x_{e,mc,in}$	$x_{e,mc,out}$	P_{in} [kPa]	Number of ΔP data points (69 total)
75.92	4005–10094	−0.031 to −0.022	0.331–0.893	688.3–690.0	4
94.90	3990–12185	−0.032 to −0.026	0.256–0.853	690.7–691.6	5
113.88	4039–16184	−0.039 to −0.025	0.206–0.956	691.5–695.0	7
132.86	4074–17999	−0.038 to −0.026	0.174–0.908	692.7–699.2	8
151.85	4003–20185	−0.038 to −0.029	0.148–0.892	693.1–704.3	9
170.83	3993–24028	−0.040 to −0.031	0.128–0.944	694.1–711.9	11
189.81	4031–26209	−0.040 to −0.030	0.111–0.928	695.0–721.4	12
208.79	4039–28209	−0.041 to −0.030	0.096–0.927	695.9–731.3	13

where q''_B is heat flux based on 609.6-mm long by 203.2-mm wide base area, A_{base}, of the heat sink, and $\dot{m}$ total flow rate of R134a. Table 3 provides detailed operating conditions tested in this study.

3. Two-phase flow dynamics and Long-term oscillations of pressure and mass velocity

3.1. Mechanism of charge transition instability (CTI) without PID control of reservoir pressure

As discussed in Section 2, maintaining a set point pressure for the two-phase loop requires simultaneous heat addition and removal from the reservoir; with electrical power supply to the reservoir's immersion heater PID controlled in response to pressure measured at the T junction downstream of the condenser. The PID control is found to have profound influence on dynamic response of the entire system, evidenced by drastically different responses with versus without PID. Discussed below is the response sans PID control.

Fig. 2 shows the system's dynamic response without PID control, starting with initial normal operating conditions with micro-channel mass velocity of G_{mc} = 208.8 kg/m^2 s and ambient air temperature of T_{amb} = 18.3 °C. Initial operating conditions for all experimental cases shared equal condenser outlet pressure, $P_{cond,out}$, set to 600 kPa. Notice, in Fig. 2(a), how, as heat flux of q''_B = 24,219 W/m^2 is applied to the micro-channel test module after 60 s, the system responds with initial increases of heat sink's inlet pressure, $P_{mc,in}$, and outlet pressure, $P_{mc,out}$, followed by periodic oscillations in both parameters. Fig. 2(b) shows corresponding initial increase followed by periodic oscillations in pressure drop, ΔP_{mc}, and both Fig. 2(a) and (b) show intermediate durations of both small amplitude and high frequency oscillations induced by *parallel channel instability* (PCI) as described in [33]. The onset of this *charge transition instability* (CTI) is also associated with synchronized oscillations in condenser inlet pressure, $P_{cond,in}$, and outlet pressure, $P_{cond,out}$, and reservoir pressure, P_{res}, as shown in Fig. 2(c). Pressure difference between $P_{cond,out}$ and P_{res} represents static head in the reservoir, ΔP_{res}. And pressure head, ΔP_{res}, measured by pressure transducers and calculated using height of liquid in reservoir obtained by level indicator are 7294.9 Pa and 7151.2 Pa, respectively, which agree quite well with one another. Notice in Fig. 2(d) how liquid height, $H_{res,f}$, increases as fluid from the loop (loop charge) moves to the reservoir, and decreases when fluid returns to the loop. Fig. 2(e) shows perhaps the most important manifestation of CTI, both periodic and severe fluctuations in micro-channel test module's mass velocity, G_{mc} starting at the moment of onset of CTI, $t_{CTI,o}$ = 380 s, following a stable initial mass velocity of G_{mc} = 208.8 kg/m^2 s. In these results, $t_{CTI,o}$ is defined by the moment when mass velocity deviates from the set value for the given test.

It is important to emphasize that CTI is fundamentally different from PCI in the former's both (1) higher oscillation amplitude and (2) lower frequency; with PCI still occurring with each oscillation period of CTI. Additionally, CTI is fundamentally different from *pressure drop oscillation* (PDO) in that CTI is associated with synchronized fluctuations of pressure drop, ΔP_{mc}, and mass velocity, G_{mc}, as opposed to unsynchronized fluctuations (*i.e.*, with finite phase shift) in the same parameters for PDO [29,48,49].

Overall, CTI is initiated in response to an increase in q''_B, which causes system pressure and void fraction in the micro-channel test module to rapidly increase. The oscillation sequence of CTI is represented in Fig. 3(a)–(d), which correspond, respectively, to times 1–4 indicated in Fig. 2(d), and can be described as follows:

(1) In the first stage of oscillation cycle, at t_1, an increase in condenser outlet pressure, $P_{cond,out}$, corresponding to set value for the loop's flow rate, $\dot{m}_{loop} = \dot{m}_{set}$, causes liquid height in the reservoir to increase as fluid charge transitions from loop to reservoir.
(2) At t_2, while still $\dot{m}_{loop} = \dot{m}_{set}$, charge transition from loop to reservoir causes liquid in the reservoir to reach threshold high level and fluid flow into the reservoir to cease.
(3) Conditions at t_2 are maintained momentarily until t_3, when the loop's mass flow rate suddenly drops, causing large vapor pockets to form in the loop because of constant heat input. This vapor is generated because the charge left in the loop is smaller than the minimum amount required for normal operation. At t_3, $P_{cond,out}$ drops suddenly, and, with ΔP_{res} (equal to $g\left(\rho_f H_{res,f} + \rho_g H_{res,g}\right)$) now high enough that liquid pressure at the bottom of the reservoir exceeds $P_{cond,out}$, fluid begins to return to the loop.
(4) Release of liquid from reservoir to loop continues until $P_{cond,out}$ begins to increase once again because of mass flow rate recovery in the loop. At t_4, liquid level reaches threshold low level. Thereafter, $P_{cond,out}$ becomes large enough once again to push liquid into the reservoir and start a new CTI oscillation cycle.

As indicated in [33] and shown in Fig. 2(b), PCI occurs in the crests of CTI and is manifest with smaller amplitude and higher frequency during normal operating conditions. The results in Fig. 2 prove that CTI and PCI occur simultaneously, but the effects of CTI on the system are far more profound in terms of both oscillation magnitude and period. Notice in Fig. 2(c) how $P_{cond,in}$ fluctuates with higher amplitude than $P_{cond,out}$ while both increase during an oscillation sequence, but they are closer to one another while they both decrease in the trough of the same sequence. This pattern of oscillation is different from that observed in the condenser of a refrigeration cycle [42] wherein normal operating conditions are intermittently maintained. In addition, while $P_{cond,in}$ and $P_{cond,out}$ in a refrigeration cycle are a quarter period out of phase, CTI in the present study shows no phase shift between the two pressures.

Overall, it appears CTI is triggered by vapor generation induced by heat addition in the test module and ensuing increase in system pressure. This observation is confirmed by comparing mass

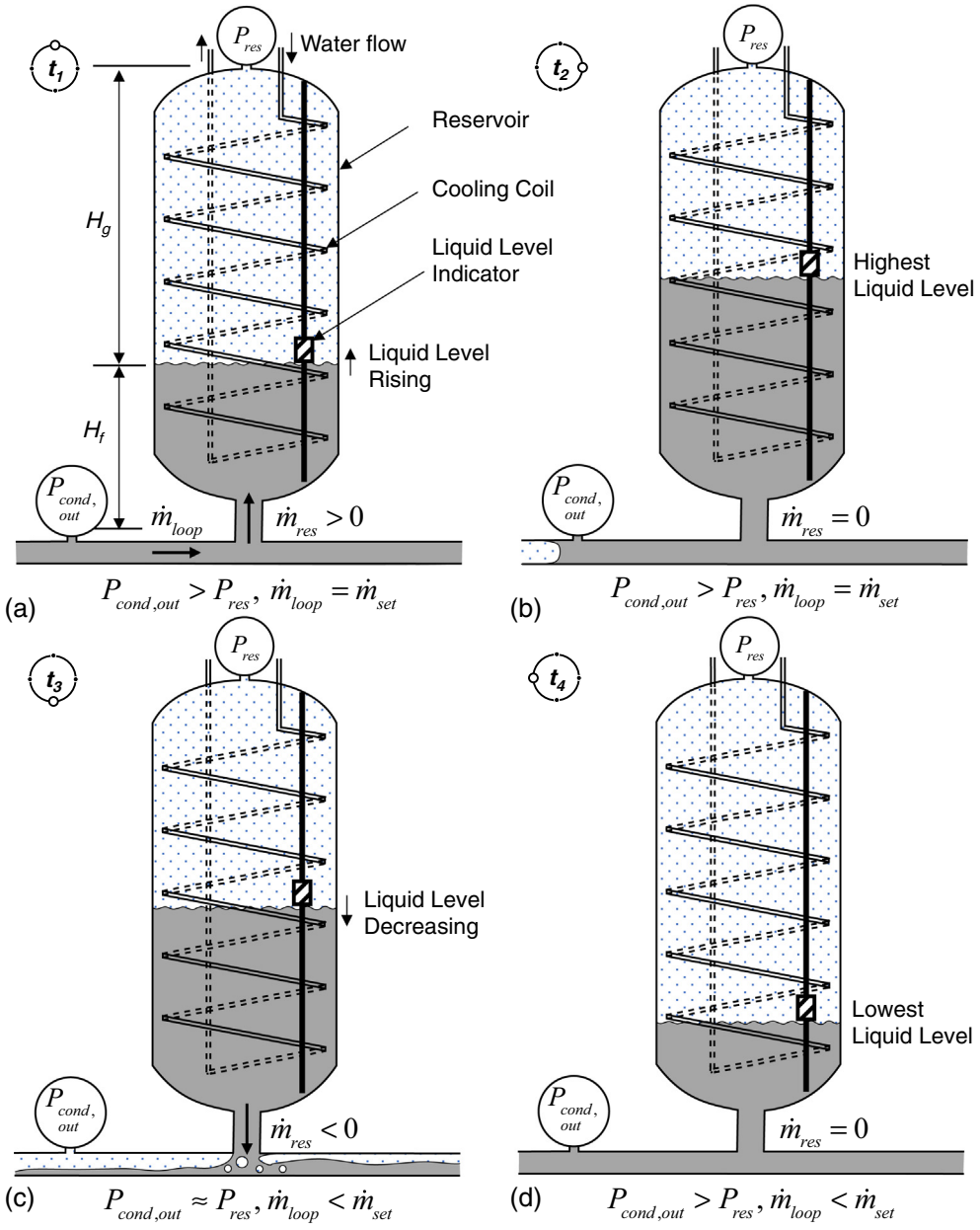

Fig. 3. Schematic representation of CTI observed when PID controller is not in use. Shown are flow behaviors in reservoir at four instances of a single periodic cycle. (a) t_1: rising liquid level due to charge transition from loop to reservoir. (b) t_2: highest liquid level corresponding to minimum charge circulating in the loop. (c) t_3: charge transition from reservoir to loop due to subnormal charge in the loop. (d) t_4: lowest liquid level before starting new cycle.

velocity responses for different heat fluxes. Fig. 4 shows, for G_{mc} = 208 kg/m^2 s (set value before instability) and T_{amb} = 18.3 °C, fluctuations in G_{mc} for q''_B = 16,146, 20,182, and 24,219 W/m^2, as q''_B is turned on at t = 58.4, 60.8 and 61.8 s, respectively. For the lowest heat flux, the onset of CTI is fairly delayed, occurring at $t_{CTI,o}$ = 2550 s, but decreases monotonically to 1420 and 380 s with increasing heat flux, proving CTI is strongly dependent on heat flux. Fig. 4(b) further supports this dependence of $t_{CTI,o}$ on heat flux for different mass velocities. Notice in the same figure that G_{mc} has relatively minor influence on CTI.

Results for loop charge, C_{loop}, defined as fluid mass in entire loop sans reservoir, are provided in Fig. 5(a) and (b). Fig. 5(a) shows temporal variations of C_{loop} for G_{mc} = 208.8 kg/m^2 s, T_{amb} = 18.3 °C, and q''_B = 16,146, 20,182, and 24,219 W/m^2. C_{loop} is shown decreasing in a gradual manner starting the instant heat flux is applied to the micro-channel heat sink, even during the period t = 0 – $t_{CTI,o}$ while G_{mc} remains fairly constant, as shown in Fig. 4(a). Comparing results in Figs. 5(a) to 4(a) corresponding to q''_B = 16,146 kW/m^2 shows C_{loop} incurs appreciable drop upon initiation of heating, while G_{mc} incurs both relatively mild and delayed response. However, CTI initiation, indicated in the G_{mc} plot, Fig. 4(a), by $t_{TCI,o}$ = 1420 and 380 s for q''_B = 20,182 and 24,219 W/m^2, respectively, precedes the onset of oscillation for C_{loop}, which is indicated in Fig. 5(a) as $t_{CTI,charge}$. In summary, $t_{CTI,o}$ is dictated by first drop in mass velocity, while $t_{CTI,charge}$ is defined by onset of oscillation in C_{loop}, and, also from Figs. 4(a) and 5(a), the difference between $t_{CTI,o}$ and $t_{CTI,charge}$ decreases with increasing q''_B. Fig. 5(b) shows $t_{CTI,charge}$ decreases monotonically with increasing q''_B, but shows minor dependence on G_{mc}.

As CTI is initiated by loss of balance in system pressure and ensuing charge transition from loop to reservoir, this instability can be described by investigating influence of total volumetric flow

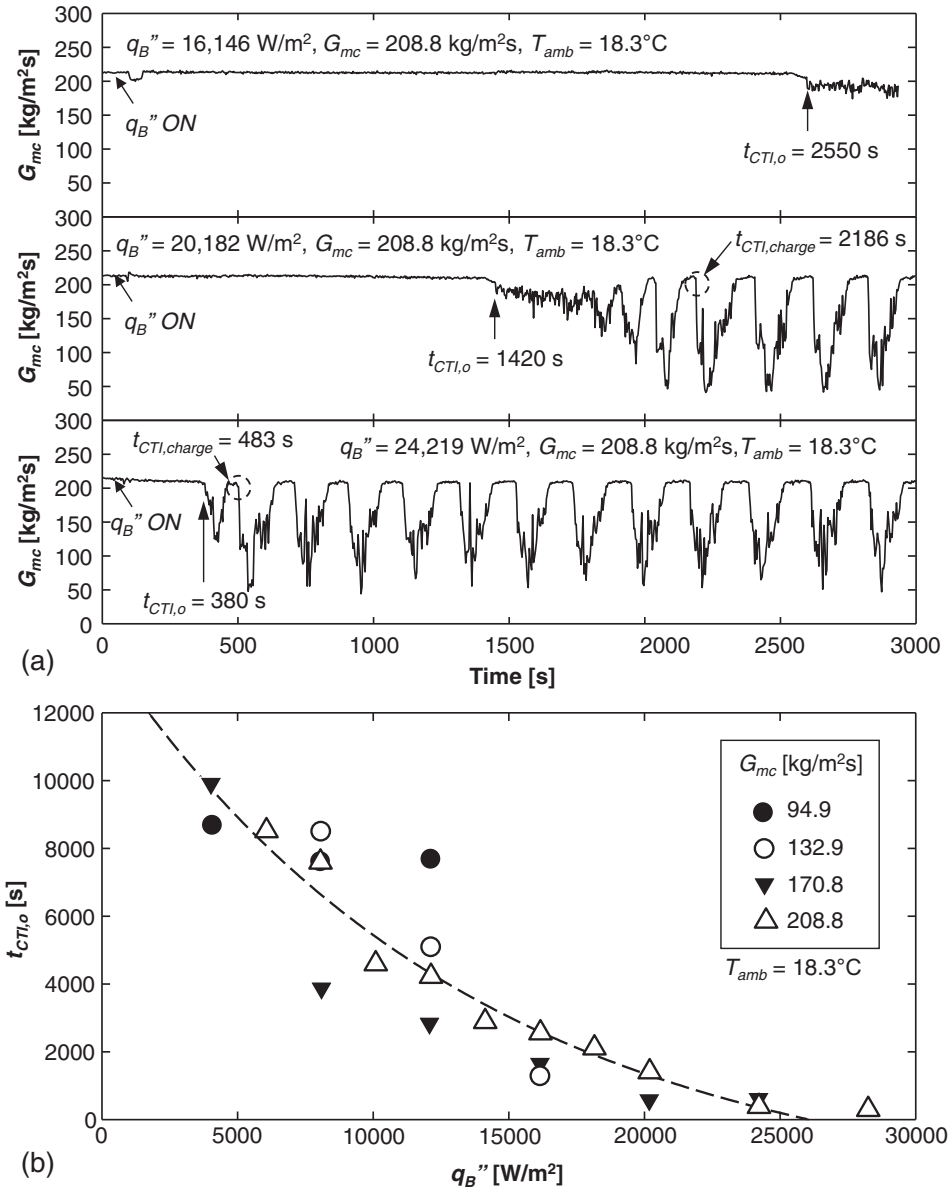

Fig. 4. Effects of micro-channel base heat flux, q_B'', on onset of CTI in absence of PID control. (a) Temporal variations of mass velocity and $t_{CTI,o}$ for G_{mc} = 208.8 kg/m² s, T_{amb} = 18.3 °C, and three heat fluxes. (b) Variations of $t_{CTI,o}$ with q_B'' for different mass velocities.

rate at the micro-channel test module's outlet on loop parameters using

$$Q_{total,out} = Q_{g,mc,out} + Q_{f,mc,out}\,, \tag{5}$$

$$Q_{g,mc,out} = \frac{A_{mc,ch}\ G_{mc}\ x_{e,mc,out}}{\rho_g} \tag{6}$$

and

$$Q_{f,mc,out} = \frac{A_{mc,ch}\ G_{mc}(1 - x_{e,mc,out})}{\rho_f}\,. \tag{7}$$

Notice that $Q_{total,out}$ increases with increasing q_B" but is far less sensitive to G_{mc}, as depicted in the inset in Fig. 6(a). Fig. 6(a) also shows time to onset of CTI, $t_{CTI,o}$, decays exponentially with increasing $Q_{total,out}$. Fig. 6(b) shows loop charge, C_{loop}, at $t_{CTI,o}$ also decreases with increasing $Q_{total,out}$ because of increasing system void fraction. It can therefore be concluded that the primary reason for CTI initiation is low C_{loop} and ensuing drop in G_{mc}. Fig. 6(c) shows condenser outlet pressure, $P_{cond,out}$, at $t_{CTI,o}$ increases with increasing $Q_{total,out}$, which expedites CTI initiation.

Fig. 7(a) shows time to initiation of C_{loop} oscillations, $t_{CTI,charge}$, decays exponentially with increasing $Q_{total,out}$, similar to the trend for $t_{CTI,o}$ in Fig. 6(a). However, Fig. 7(b) shows C_{loop} at $t_{CTI,charge}$, unlike Fig. 6(b), remains fairly constant with increasing $Q_{total,out}$, and the magnitude of C_{loop} is smaller than at $t_{CTI,o}$. Fig. 7(c) shows $P_{cond,out}$ increases gradually with increasing $Q_{total,out}$ with a certain extent of scattering, which is caused by pre-sustained pressure oscillation from $t_{CTI,o}$ in the vicinity of $t_{CTI,charge}$. Notice, by comparing Figs. 6(a) and 7(a), that at high $Q_{total,out}$, $t_{CTI,o}$ and $t_{CTI,charge}$ approach one another, so do corresponding values for C_{loop} in Figs. 6 (b) and 7(b).

3.2. Mechanism of charge transition instability (CTI) with PID control of reservoir pressure

With PID control of electrical power supply to the reservoir's immersion heater in response to pressure at the condenser outlet,

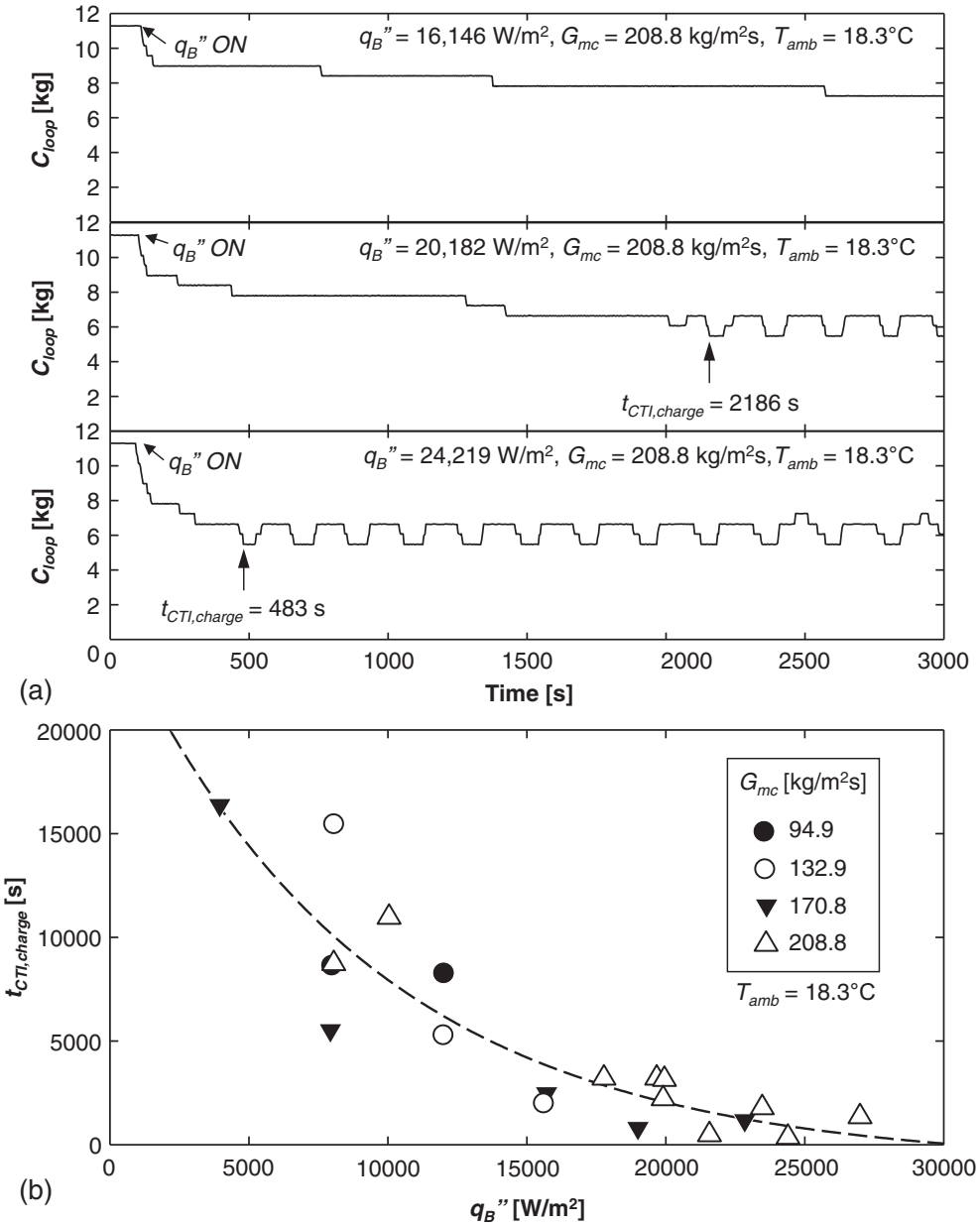

Fig. 5. Effects of micro-channel base heat input, q_B'', on $t_{CTI,charge}$ in absence of PID control. (a) Temporal variations of C_{loop} and $t_{CTI,charge}$ for G_{mc} = 208.8 kg/m² s, T_{amb} = 18.3 °C, and three heat fluxes. (b) Variations of $t_{CTI,charge}$ with q_B'' at different mass velocities.

$P_{cond,out}$, the system is clearly better able to tackle fluctuations in operating parameters. The role of PID control is captured by comparing temporal records of G_{mc} and C_{loop} after CTI is initiated for the same operating conditions of G_{mc} = 208.8 kg/m² s and q_B'' = 20,182 W/m² without PID control, Fig. 8(a), and with PID control, Fig. 8(b). For the case without PID control, Fig. 8(a), G_{mc} shows relatively minor fluctuation when q_B'' is turned on at 123.3 s, but C_{loop} begins to decrease gradually as the charge begins to move into the reservoir. Mild instability is initiated at $t_{CTI,o}$ = 2284 s where C_{loop} = 7.232 kg, which is followed by sharp instability at $t_{CTI,charge}$ = 3156 s where C_{loop} = 6.103 kg. Flow oscillation is maintained until the end of data recording at 7000 s as shown in the Fig. 8(a) inset, with C_{loop} fluctuating between 6.103 and 7.811 kg.

Fig. 8(b) shows how oscillations are suppressed and system returns to normal operation once the PID controller is turned on. For this case, the PID controller is triggered once $P_{cond,out}$ falls below P_{set} = 571.8 kPa, which corresponds to mass velocity below G_{mc} = 77.0 kg/m² s, and responds by rapidly increasing power input to the reservoir's immersion heater. This causes vigorous vapor generation to push liquid back to the loop. The mass flow rate is stabilized and returns to normal operation with G_{mc} = 208.8 kg/m² s, as C_{loop} also recovers from oscillation at t = 3924 s, rising to a stable value of 7.802 kg.

Fig. 9(a) shows temporal records of G_{mc}, C_{res} (reservoir charge), $P_{cond,out}$, and P_{res} both before and after CTI with the PID controller in use. Here, $P_{cond,out}$ is initially at 600 kPa and decreases in response to PID control, set at P_{set} = 571.8 kPa, to equilibrium pressure of P_{equil} = 564.5 kPa, which is defined as $P_{cond,out}$ at $t_{CTI,o}$, and whose magnitude is determined from operating conditions and ambient temperature, T_{amb}.

Fig. 9(a) shows the temporal span divided into four distinct periods (1–4) corresponding to four oscillation sequences, with behavior within each captured in Fig. 10, which can be described as follows:

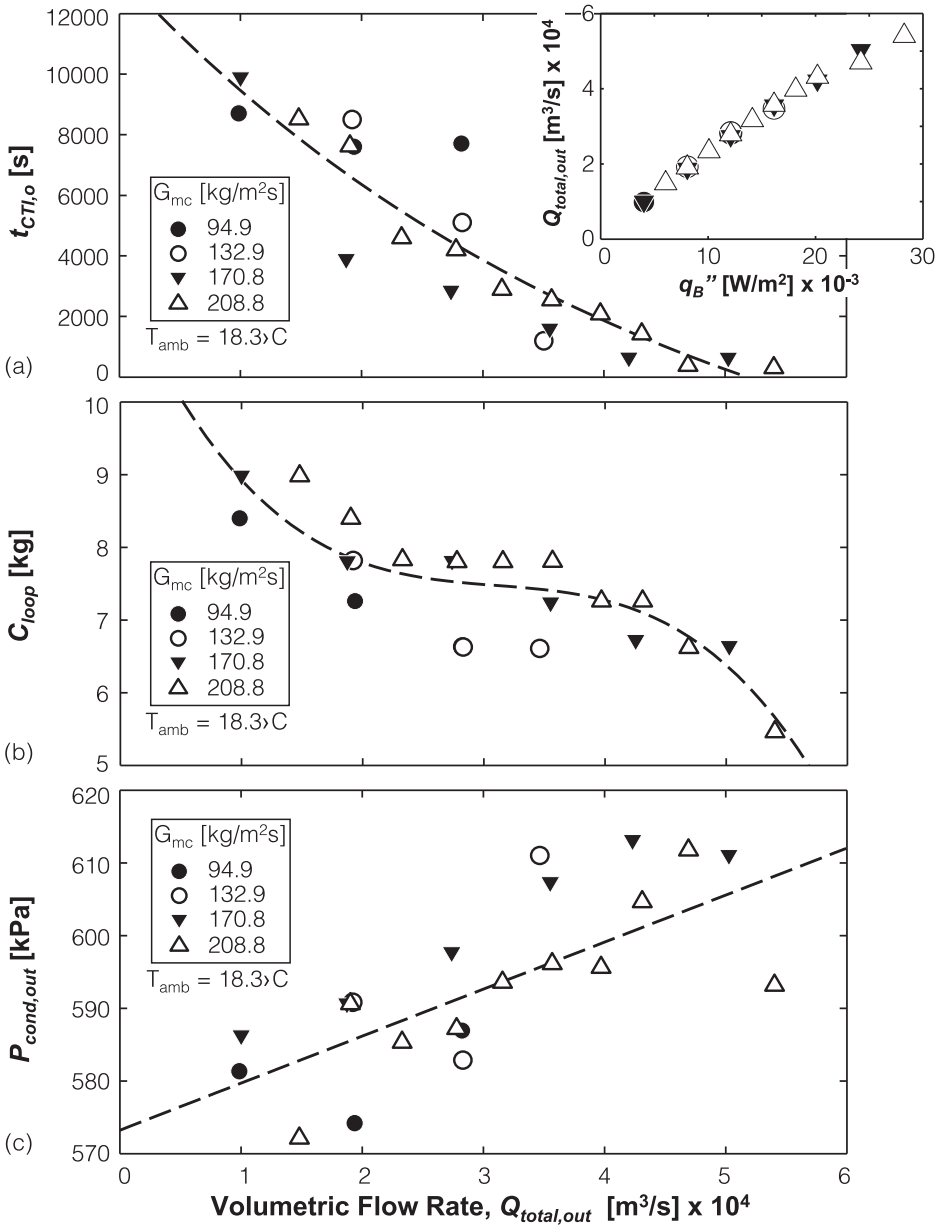

Fig. 6. Effects of volumetric flow rate at micro-channel test module's outlet, $Q_{total,out}$, on (a) $t_{CTI,o}$, (b) C_{loop}, and (c) $P_{cond,out}$ for T_{amb} = 18.3 °C at the onset of CTI with different mass velocities.

(1) During t_1, $P_{cond,out}$ and P_{res} decrease simultaneously after q''_B is turned on until $P_{cond,out}$ reaches P_{equil}, during which time C_{res} rapidly increases. Then, liquid charge transitions from loop to reservoir, and the increase in C_{res} slows.

(2) At t_2, liquid in the reservoir reaches highest level, and, simultaneously, reduced loop charge increases vapor generation in the loop.

(3) Reduced loop charge now triggers sharp drop in the loop's mass velocity, and, at t_3, the PID controller turns on after $P_{cond,out}$ drops below P_{set} by a finite amount, which corresponds to when G_{mc} drops below 77.0 kg/m^2 s. A sudden surge of power to the reservoir's heater now triggers appreciable boiling in the reservoir, which begins to push liquid back to the loop, causing a decrease in C_{res}. The PID control also causes both $P_{cond,out}$ and P_{res} to start rising.

(4) At t_4, the PID control ultimately causes G_{mc} to recover to set operating value, and $P_{cond,out}$ to be maintained thereafter very close to P_{set} by maintaining correct amount of vapor generation in the reservoir.

It is also important to emphasize that the closed loop's saturation pressure is influenced by ambient temperature, which, along with P_{set} value, might interfere with ability of the PID controller to suppress oscillations. This complex relationship is made clearer by comparing conditions for Fig. 9(a) and (b), which correspond to nearly identical values of P_{equil}, 564.5 versus 566.8 kPa, because of only 0.1 °C difference in T_{amb}.

In Fig. 9(a), P_{set} = 571.8 kPa, which is higher than P_{equil} = 564.5 kPa. In Fig. 9(b), however, P_{set} = 563.0 kPa, lower than P_{equil} = 566.8 kPa. While those pressure differences may seem small, successful removal of oscillations with PID control in Fig. 9

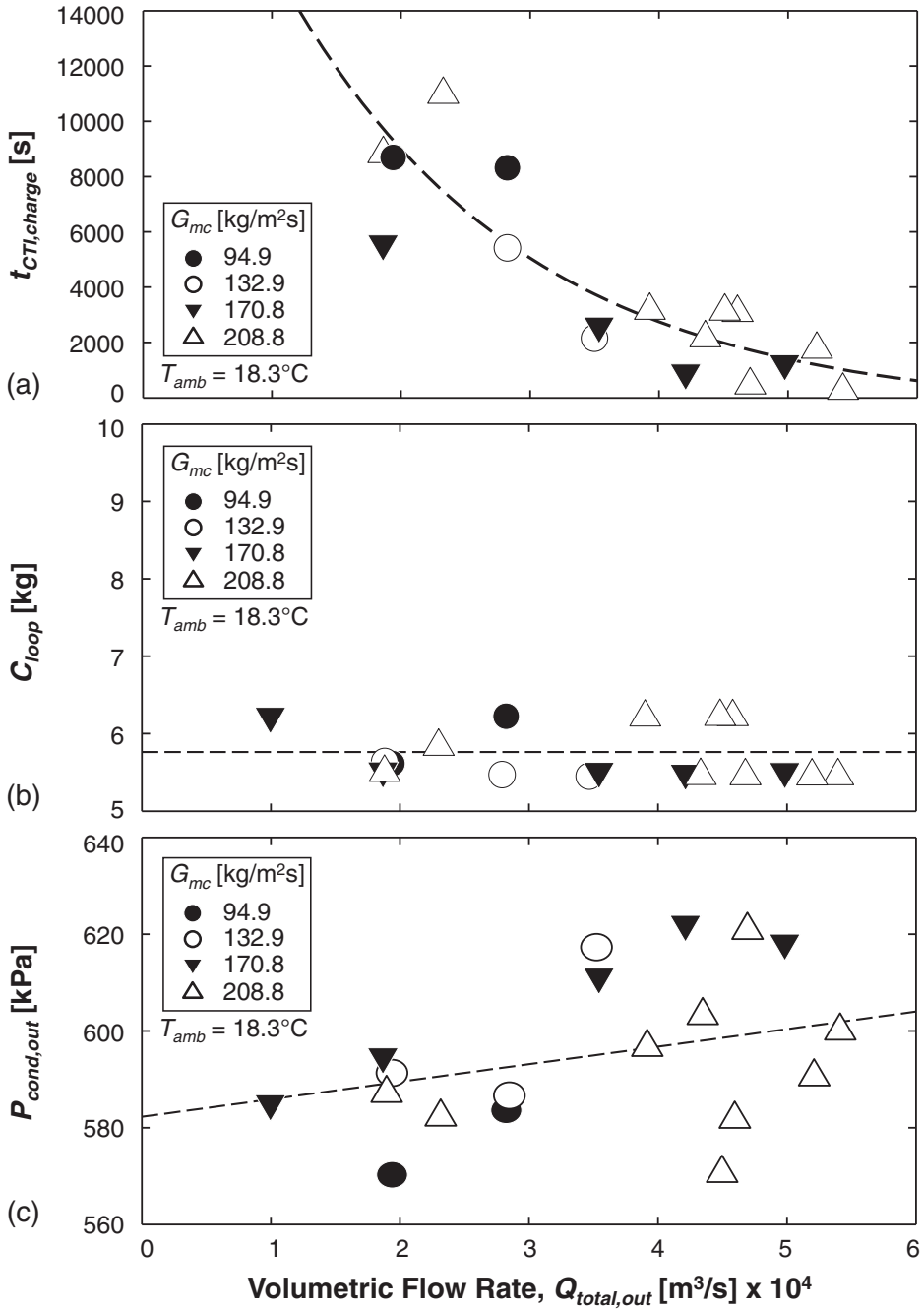

Fig. 7. Effects of volumetric flow rate at micro-channel test module's outlet, $Q_{total,out}$, on (a) $t_{CTI,charge}$, (b) C_{loop}, and (c) $P_{cond,out}$ for T_{amb} = 18.3 °C and different mass velocities in absence of PID control.

(a) versus its failure in Fig. 9(b) shows that proper operation requires setting P_{set} higher than P_{equil} in order for the PID controller to be able to return charge to the loop.

Turning attention to the influence of ambient temperature on system behavior, Fig. 11 shows strong monotonic increasing dependence of P_{equil} on T_{amb}. There are also secondary effects of G_{mc} and q''_B, with the latter providing measurable influence (albeit weaker than that of T_{amb}) as shown in the inset corresponding to $T_{amb} \approx 17.0$ °C.

Since, as discussed above, successful implementation of PID control is dictated by the relative magnitude of P_{equil} and P_{set}, variations of the former with T_{amb} imply that T_{amb} also has strong influence on PID function. This fact is reflected in Fig. 12(a), which shows temporal records of $P_{cond,out}$ for G_{mc} = 208.8 kg/m^2 s, q''_B = 24,219 W/m^2, P_{set} = 646.0 kPa, and two different ambient temperatures, 19.9 °C and 15.2 °C. With the higher T_{amb} resulting in higher P_{equil} of 670 kPa, which is higher than P_{set}, no system stability is achieved after CTI initiation. On the other hand, the lower T_{amb} decreases P_{equil} to 590 kPa, which is now smaller than P_{set}, enabling the PID controller to prevent ensuing oscillations.

Some guidance concerning safe operation can be achieved with the aid of a stability map, shown in Fig. 12(b) for G_{mc} = 208.8 kg/m^2 s and q''_B = 24,219 W/m^2. Operation shifts from unstable to stable in response to changes in T_{amb} for a given value of P_{set}. Notice how stable operation favors lower T_{amb} and higher P_{set}. However, higher P_{set} would also increase saturation temperature, $T_{mc,sat}$, in

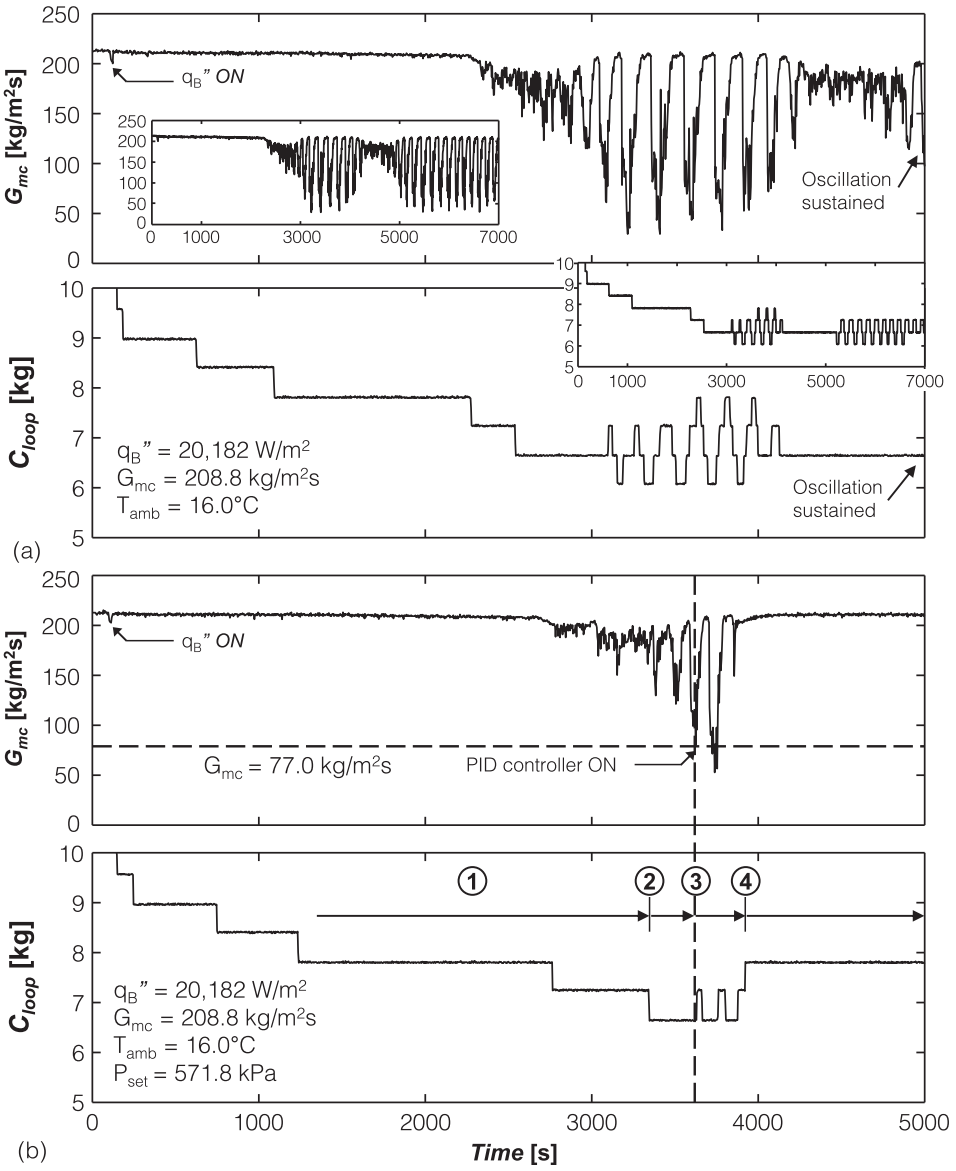

Fig. 8. Temporal records of mass velocity, G_{mc}, and loop charge, C_{loop}, before and after CTI for q_B'' = 20,182 W/m², G_{mc} = 208.8 kg/m² s, and T_{amb} = 16.0 °C (a) without PID control, and (b) with PID control (based on P_{set} = 571.8 kPa).

the micro-channel test module, which would influence heat transfer performance.

4. Effects of charge transition instability (CTI) on thermal response of Micro-channel heat sink

Attention will now shift to impact of CTI on temperature distribution and changes in two-phase heat transfer mechanisms along the heat sink. Recall that heat sink temperature is measured by 10 thermocouples (*tc2* to *tc11*, situated at axial locations indicated in Table 1). Fig. 13(a) shows temperature records for a select subset of thermocouples situated at z = 102.1, 217.9, 333.8, 434.3, and 565.4 mm over an extended duration of t = 0–10,000 s, starting the instant the heat sink's heater is turned on. The conditions shown are for a test with PID control that satisfies the stability criterion discussed in the previous section. Notice how the temperature fluctuations are suppressed significantly at $t_{sup} \approx$ 7402 s, and reach normal operation at $t_{norm} \approx$ 8000 s. Normal operation is sustained thereafter by maintaining $P_{cond,out}$ below P_{set} and G_{mc} constant. Prior to reaching normal operation, G_{mc} fluctuates significantly, Fig. 13(b), causing appreciable fluctuations in heat sink temperature. Notice in the same figure the synchronous temperature rise for durations of low G_{mc}, Fig. 13(c), which promotes dryout along the micro-channels, and temperature drop for high G_{mc} and surface rewetting, with temperature amplitude increasing downstream because of axially increasing void fraction exasperating dryout for downstream locations.

Large axial differences in temperature response are clearly manifest when comparing temporal records for downstream thermocouples T_{tc7} – T_{tc11} (z = 333.8–565.4 mm) with those for upstream thermocouples T_{tc2} – T_{tc6} (z = 44.2–275.8 mm), with larger amplitudes reflecting much weaker cooling downstream. Highest amplitude of 18.7 °C is detected with T_{tc9}, presumably because of more persistent dryout at this location. Additionally, while T_{tc7} – T_{tc11} increase during the period of decreasing G_{mc}, those for T_{tc2} – T_{tc6} actually decrease. Strongly associated with these temperature differences are differences in dominant heat transfer mechanism. Large heat transfer coefficients are realized upstream because of reliance on nucleate boiling with low void fraction (as confirmed

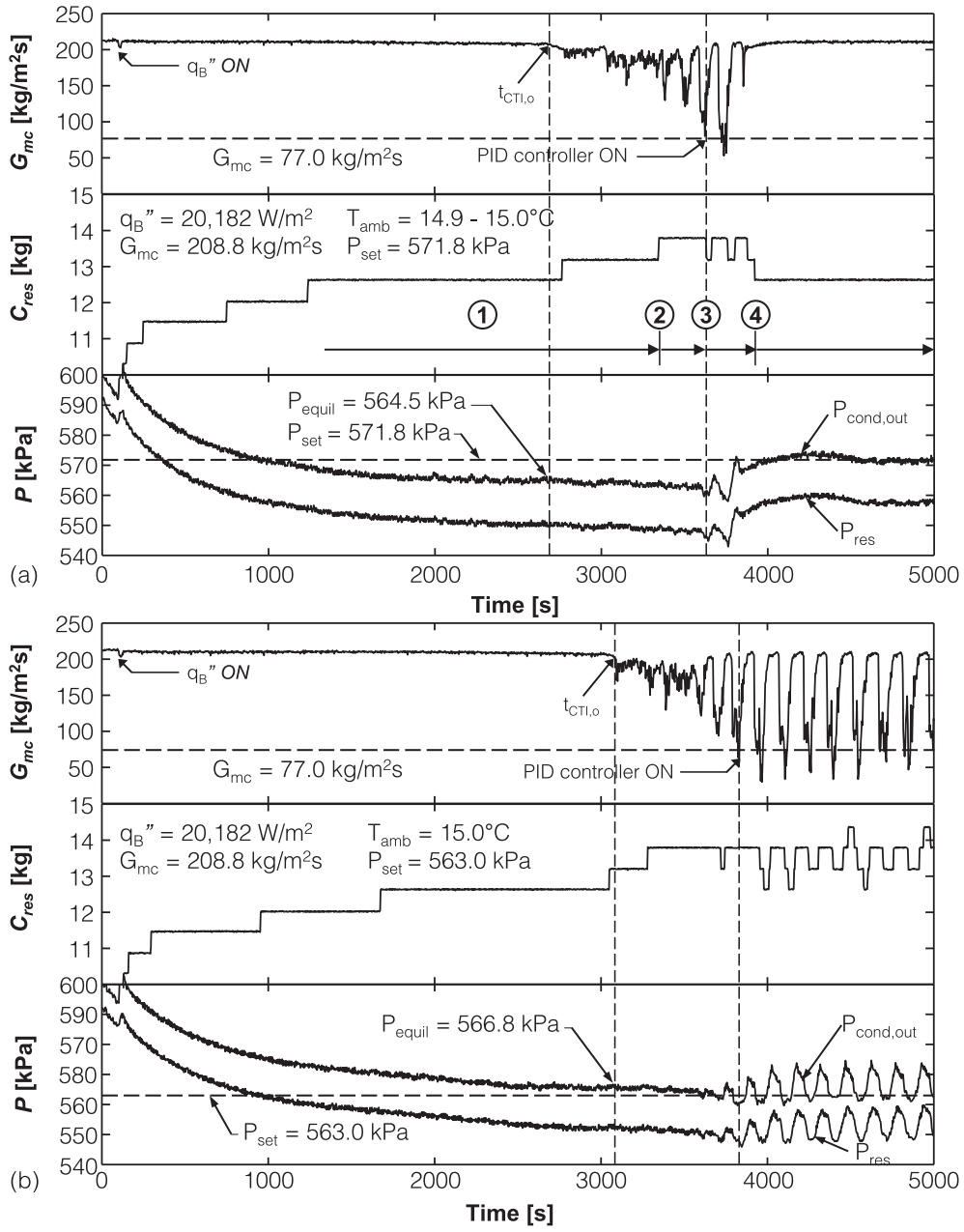

Fig. 9. Temporal records of G_{mc}, C_{res}, $P_{cond,out}$, and P_{res} with PID control for conditions leading to (a) successful suppression of oscillations following CTI when $P_{set} > P_{equil}$, and (b) unsuccessful suppression when $P_{set} < P_{equil}$.

in prior studies by the present authors [34]), while low coefficients are achieved downstream because of high void fraction, reliance on convective boiling across an annular film, and increased likelihood of dryout. Overall, the downstream regions are prone to encountering localized CHF earlier, and CTI may yield much smaller CHF values compared to CHF resulting from intermittent downstream dryout under normal operating conditions [34,50].

The inset in Fig. 13(b) provides another important observation of synchronous response of heat sink's upstream temperatures and corresponding local saturation temperatures, T_{sat}; the latter fluctuate in accordance with local saturation pressure, P_{sat}. However, the downstream temperatures are observed to be insensitive to local T_{sat}.

It should be emphasized that within the 'slow' cyclical charge transition instability (CTI) and even during ensuing normal operation the high frequency fluctuations resulting from parallel channel instability (PCI) exists, which are associated with intermittent dryout. Shown in Fig. 13(a), the largest increases in heat sink temperature resulting from CTI and PCI are 30 °C and 5 °C, respectively, which demonstrates the relative importance of CTI over PCI.

While large temperature fluctuations induced by mass velocity oscillation during CTI may seem similar to those resulting from pressure drop oscillation (PDO) [51], they are fundamentally different from PDO in terms of (a) synchronous oscillations of mass velocity and pressure drop for CTI as opposed to out of phase oscillations for PDO, and (b) ability of system incurring CTI to reach normal operation (albeit after a long waiting period and with persistent low amplitude PCI) compared to sustained instability for PDO.

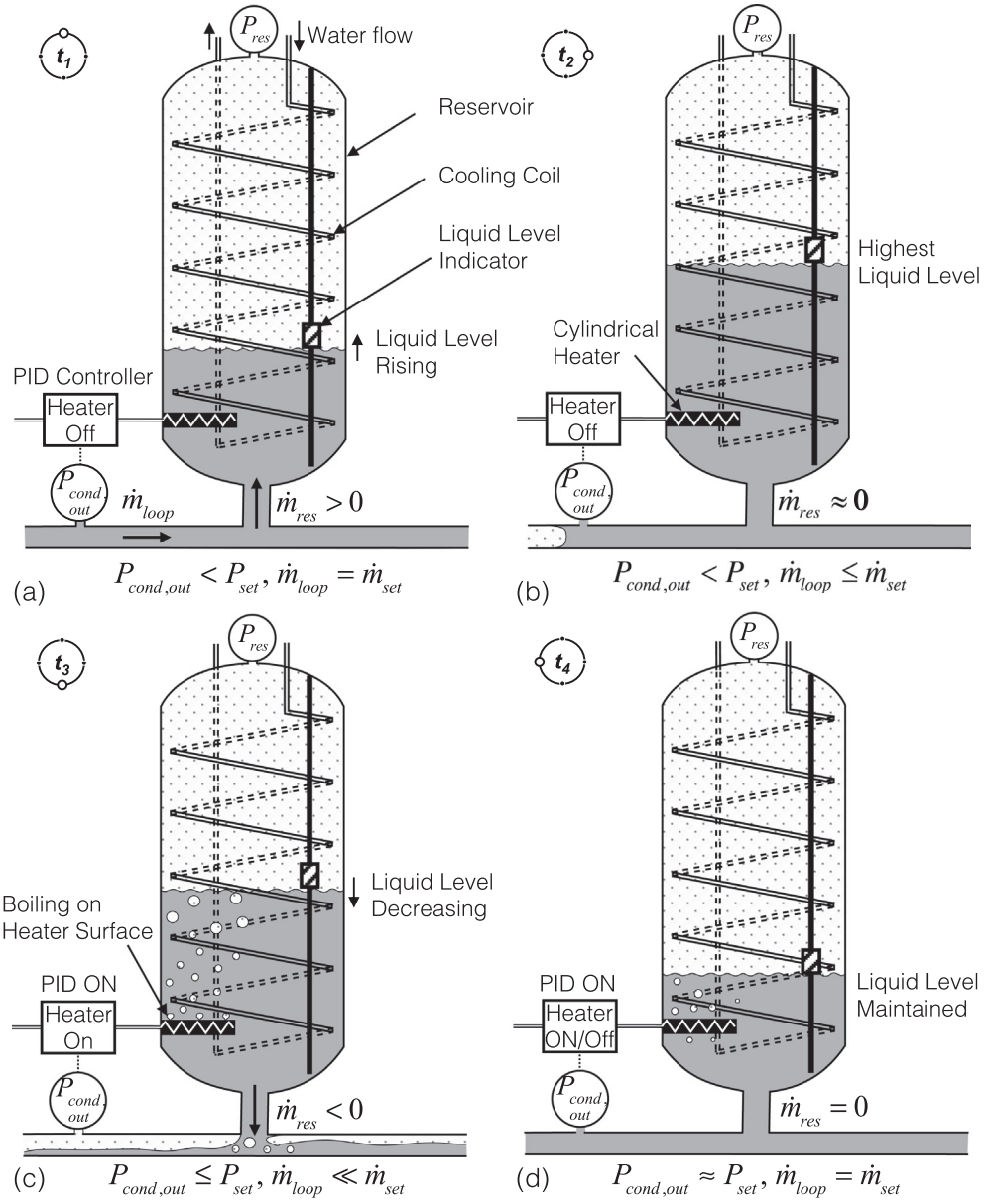

Fig. 10. Schematic representation of CTI observed with use of PID controller when $P_{set} > P_{equil}$. Shown are flow behaviors in the liquid reservoir at four instance: (a) t_1: rising liquid level due to charge transition from loop to reservoir, (b) t_2: highest liquid level corresponding to minimum charge circulating in the loop, (c) t_3: charge transition from reservoir to loop as heater power is turned on by PID controller, and (d) t_4: lowest liquid level attained when heater is turned off.

5. Charge transition instability (CTI) versus pressure drop oscillation (PDO)

5.1. Characteristics curve for CTI

Prior investigators [35,37,48,49,52,53] used characteristics curves represented by pressure drop versus mass velocity to predict occurrence of instabilities, static or dynamic, in the region of negative slope,

$$\frac{d(\Delta P)}{dG} < 0 \tag{8}$$

To investigate possible applicability of the same criterion to CTI, present transient experimental data are plotted in Fig. 14(a) and (b) to generate internal characteristics (ΔP_{mc} versus G_{mc}) superimposed on steady-state trends. Fig. 14(a) shows steady-state characteristics curves (after instability suppression with PID control), both experimental and predicted, for different heat fluxes. The pressure drop predictions are based on a technique detailed in a previous paper by the present authors [43]. Shown in Fig. 14(a) are values for total pressure drop, which is comprised of components representing single-phase liquid, two-phase mixture, and single-phase vapor,

$$\Delta P_{total} = \Delta P_{sp,f} + \Delta P_{tp} + \Delta P_{sp,g} \tag{9}$$

Notice slope change for each heat flux with decreasing G_{mc}, which is brought about by the flow in the micro-channel's downstream region switching from two-phase mixture ($\Delta P_{sp,g}$=0) to superheated vapor ($\Delta P_{sp,g}$>0). The exit condition for all present experimental data is saturated mixture, with G_{mc} values exceeding those corresponding to $x_{e,mc,out}$ = 1. Absent from all characteristics curves in Fig. 14(a) are any saturated mixture regions with

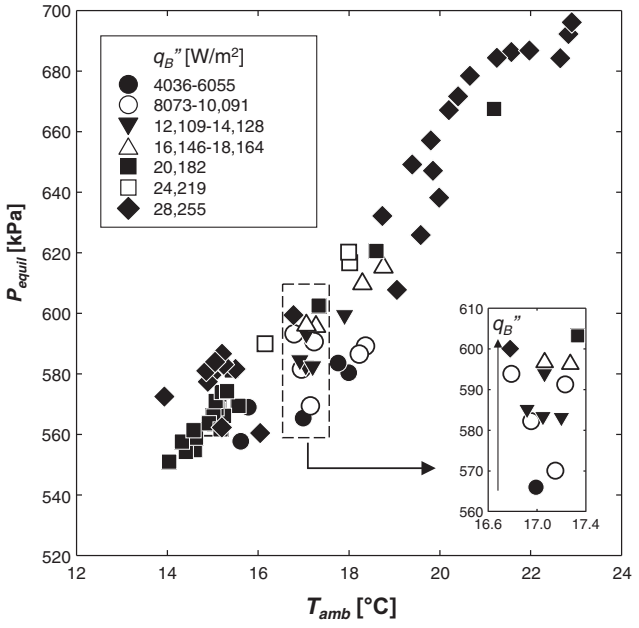

Fig. 11. Variations of equilibrium pressure, P_{equil}, with ambient temperature, T_{amb}, for G_{mc} = 94.9–208.8 kg/m² s and q_B'' = 4036–28,255 W/m².

negative slope. This can be interpreted by the increase in G_{mc} increasing $(dP/dz)_{tp}$ faster than the decrease in length of two-phase mixture region.

As discussed in Section 3, all present experimental data without PID control produced CTI. Fig. 14(b) compares, for three sets of conditions, transient experimental CTI data recorded during three consecutive cycles from the first oscillation with analytically predicted steady-state characteristics. Notice, for all three conditions, that CTI data feature only positive slope, similar to that predicted numerically, which is opposite to the negative slope trend observed with PDO, implying oscillations observed in the present study are mechanistically different than those observed in the vast majority of prior negative slope based studies [48,49].

5.2. Characteristics curve for PDO

To contrast CTI behavior from that of PDO, prior experimental conditions for water flow boiling in a micro-channel heat sink by Qu and Mudawar [29] are plotted in Fig. 15 alongside numerical predictions for steady-state operation using identical operating conditions. It should be noted that Qu and Mudawar were able to suppress PDO by throttling flow upstream of the heat sink in order to isolate the heat sink from the loop's upstream compressible volume, but the data region shown in Fig. 15 was measured under PDO without the upstream throttling. Two sets of numerical predictions are shown, one by Qu and Mudawar [29] and the other Kim and Mudawar [54,55]; both have been selected for superior predictive accuracy compared to other methods [43]. Notice that measured center of PDO falls almost exactly on the characteristics predicted by Kim and Mudawar. The clockwise data trajectory under PDO is clearly identified along negative slope of the characteristics curve, which is directly opposite that of CTI. This points to PDO and CTI following fundamentally different mechanisms.

6. Prediction of onset of charge transition instability (CTI)

Charge transition is an important manifestation of two-phase flow systems reported in previous investigations [28,56,57]. Instability resulting from this transition is fundamentally different from PDO in that the CTI can suddenly occur during steady-state operation in the form of oscillations in both mass velocity and pressure. It is therefore important from a practical standpoint to unveil the trigger mechanisms behind this phenomenon to ensure proper operation of a two-phase cooling system.

The assumption used here is that CTI commences once the amount of charge held in the loop falls below the minimum required for normal operation,

$$C_{loop} < C_{loop,min}\,. \tag{10}$$

Following is a detailed charge calculation procedure, which is conducted to both help understand the mechanism for CTI and corresponding minimum charge responsible for initiating the instability in a two-phase loop fitted with PID control. It is important to emphasize that, in the analysis presented here, the condenser's air-side heat transfer coefficient, h_{air}, is held constant during the CTI occurrence.

6.1. Charge calculation for micro-channel heat sink

Total charge in the micro-channel heat sink, C_{mc}, is comprised of charges associated with inlet plenum, $C_{mc,in}$, micro-channels, $C_{mc,ch}$, and outlet plenum, $C_{mc,out}$,

$$C_{mc} = C_{mc,in} + C_{mc,ch} + C_{mc,out}\,. \tag{11}$$

And, $C_{mc,ch}$ is, in turn, the sum of charges of upstream single-phase liquid, $C_{mc,sp,f}$, two-phase region, $C_{mc,tp}$, and, when present, outlet single-phase vapor, $C_{mc,sp,g}$,

$$C_{mc,ch} = C_{mc,sp,f} + C_{mc,tp} + C_{mc,sp,g}\,. \tag{12}$$

The single-phase subcooled liquid charge is calculated from

$$C_{mc,sp,f} = A_{mc,ch}\int_0^{L_{sp,f}} \rho_f dz\,, \tag{13}$$

where $A_{mc,ch}$ is total cross-sectional area of micro-channels, and $L_{sp,f}$ length of single-phase liquid region, which is expressed as

$$L_{sp,f} = \frac{G_{mc}A_{mc,ch}}{N_{ch}\,q_B''(W_{ch}+2\ W_w)}c_{p,f}\left(T_{sat,in}-T_{f,in}\right), \tag{14}$$

where N_{ch}, W_{ch}, W_w, $T_{sat,in}$, and $T_{f,in}$ are, respectively, number of parallel micro-channels, micro-channel width, half-width of copper wall separating micro-channels, inlet saturation temperature, and inlet liquid temperature. With base heat flux, q_B'', held constant during CTI, local thermodynamic equilibrium quality along the channels can be determined from the relation

$$x_{e,mc,z} = x_{e,mc,in} + \frac{q_B''(W_{ch}+2\ W_w)}{G_{mc}\,A_{mc,ch}\,h_{fg}}\,z. \tag{15}$$

The two-phase region charge is calculated as

$$C_{mc,tp} = A_{mc,ch}\int_{L_{sp,f}}^{L_{sp,f}+L_{tp}} \Big(\rho_g\alpha_z + \rho_f(1-\alpha_z)\Big)dz\,, \tag{16}$$

$$L_{tp} = \frac{G_{mc}A_{mc,ch}h_{fg}}{N_{ch}(W_{ch}+2W_w)q_B''}\quad, \tag{17}$$

$$A_{mc,ch} = N_{ch}\ H_{ch}\ W_{ch}\,, \tag{18}$$

and α_z is local void fraction in the two-phase region, which is calculated using Zivi's [58] correlation,

$$\alpha_z = \left[1+\left(\frac{1-x_{e,mc,z}}{x_{e,mc,z}}\right)\left(\frac{\rho_g}{\rho_f}\right)^{2/3}\right]^{-1}, \tag{19}$$

which showed good accuracy in predicting accelerational pressure drop in a previous study by the present authors [43].

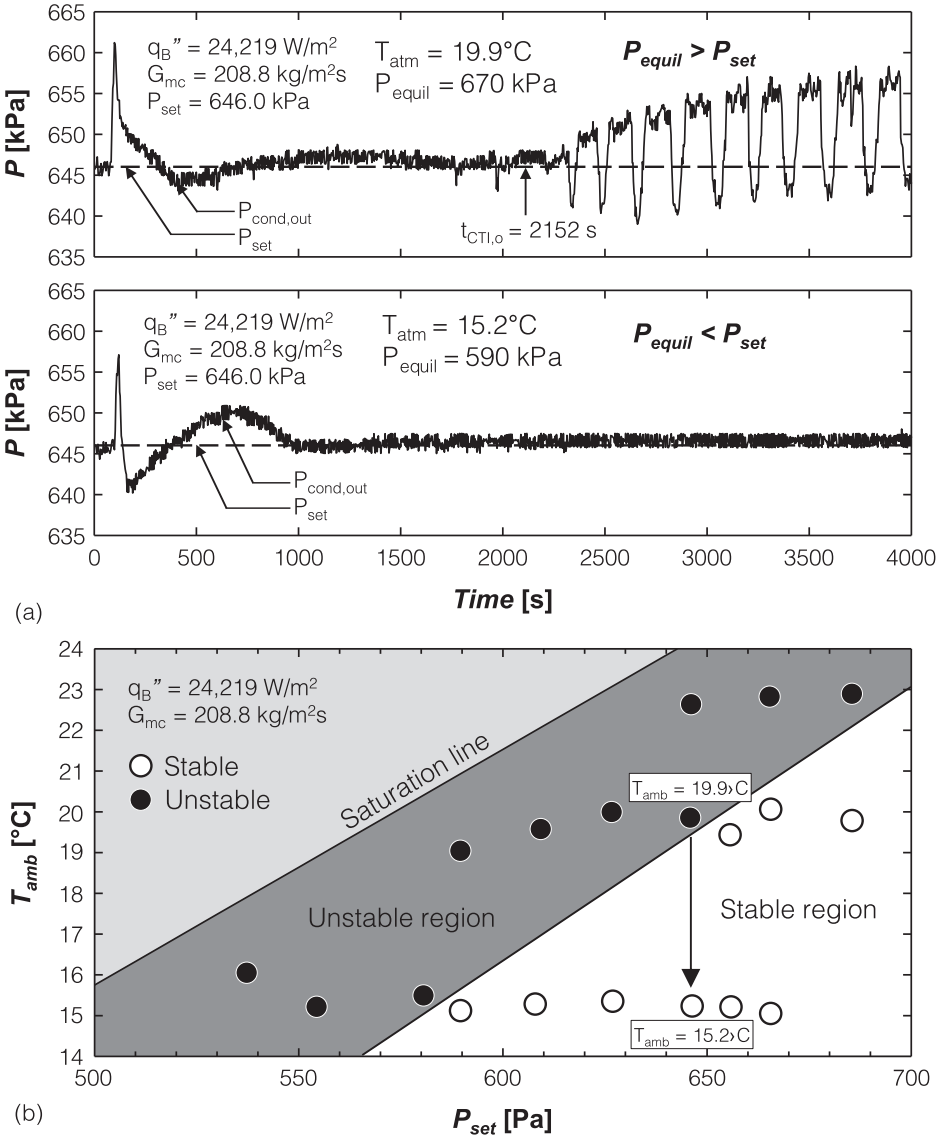

Fig. 12. (a) $P_{cond,out}$ responses for G_{mc} = 208.8 kg/m^2 s, q_B'' = 24,219 W/m^2, and P_{set} = 646 kPa with use of PID controller, culminating in system destabilization for T_{amb} = 19.9 °C and stable operation for T_{amb} = 15.2 °C. (b) T_{amb} versus P_{set} stability map for same mass velocity and heat flux.

Charge for single-phase superheated vapor is calculated as

$$C_{mc,sp,g} = A_{mc,ch} \int_{L_{sp,f}+L_{tp}}^{L_{ch}} \rho_g dz\,, \tag{20}$$

where L_{ch} is total channel length and

$$L_{sp,g} = L_{ch} - L_{sp,f} - L_{tp}\,. \tag{21}$$

Charges in the inlet and outlet plenums are calculated as

$$C_{mc,in} = \left[\rho_g \alpha_{in} + \rho_f (1-\alpha_{in})\right]\ V_{plenum,in} \tag{22}$$

and

$$C_{mc,out} = \left[\rho_g \alpha_{out} + \rho_f (1-\alpha_{out})\right] V_{plenum,out}\,, \tag{23}$$

where α_{in}, α_{out}, $V_{plenum,in}$, and $V_{plenum,out}$ are, respectively, void fraction in upstream plenum, void fraction in downstream plenum, volume of upstream plenum, and volume of downstream plenum.

Charge in the loop between micro-channel module and condenser is calculated according to

$$C_{mc-cond} = \left[\rho_g \alpha_{out} + \rho_f (1-\alpha_{out})\right]\ V_{mc-cond}\,, \tag{24}$$

where $V_{mc\text{-}cond}$ is total fluid volume of loop components separating micro-channel module and condenser, within which both $x_{e,mc,out}$ and α_{out} are assumed constant because of minimal heat loss to ambient.

6.2. Charge calculation for air-cooled condenser

Details of resistances and heat transfer coefficient relations for both condensing fluid and air are provided in Appendix A.

As indicated in Appendix A and depicted in Fig. A1(b), total thermal resistance between fluid inside the condensing tube and ambient air is given by

$$R_{total} = \frac{T_{cond} - T_{amb}}{q''_{cond}(2\pi\ r_i)\Delta z} = \frac{1}{h_{cond}\ (2\pi\ r_i)\Delta z} + \frac{\ln(r_o/r_i)}{2\ \pi\ k_w\ \Delta z} + R_{equiv}, \tag{25}$$

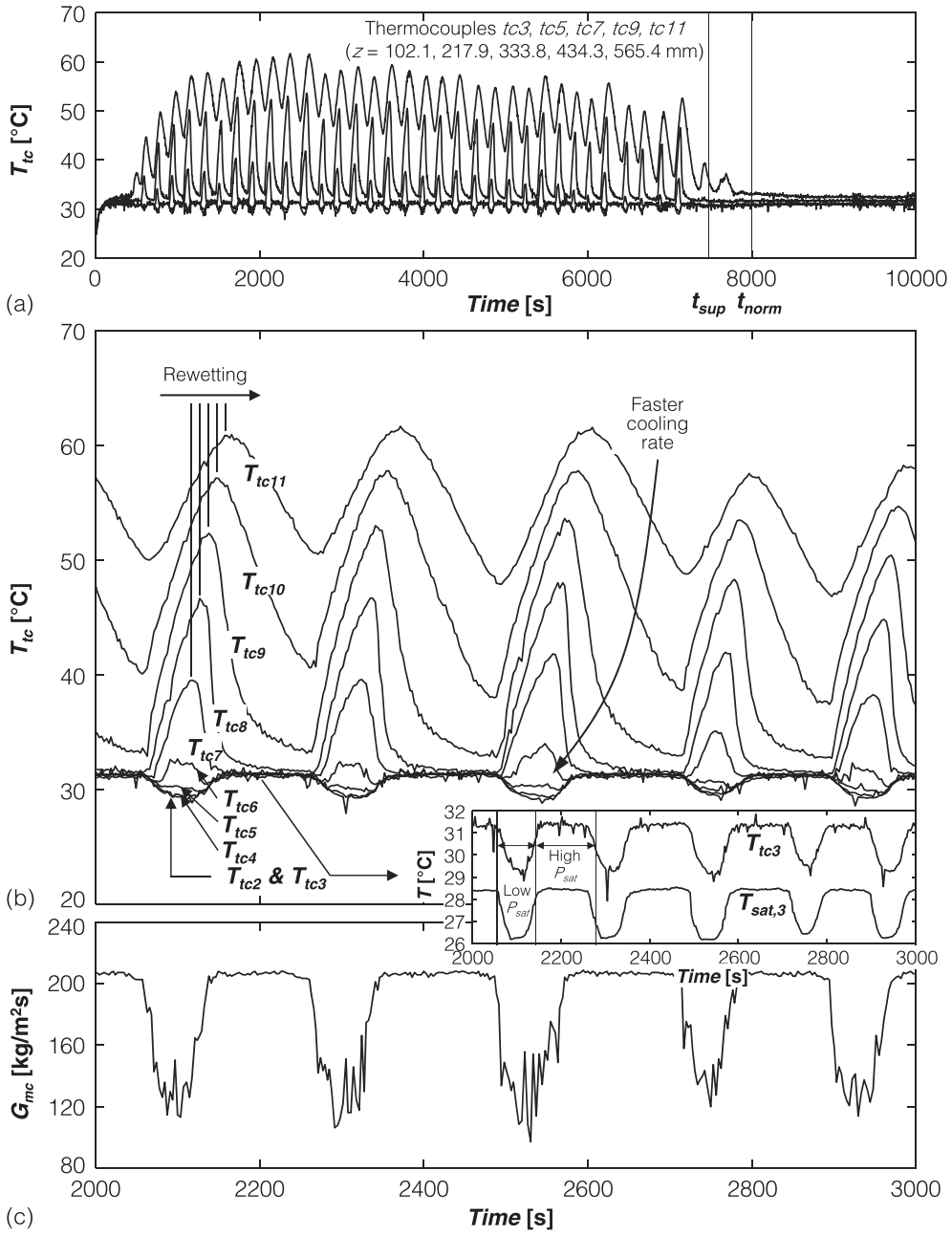

Fig. 13. Thermal effects of CTI on thermal response of micro-channel heat sink with use of PID control for q_B'' = 28,255 W/m^2 and G_{mc} = 208.8 kg/m^2 s: (a) Temporal response of representative heat sink thermocouples until full restoration of steady operating conditions. (b) Temperature response of all heat sink thermocouples during CTI. (c) Temporal response of mass velocity during CTI.

where R_{equiv} is equivalent airside thermal resistance accounting for both finned and bare portions of tube surface, and T_{cond} and h_{cond} are, respectively, the temperature and heat transfer coefficient of internal condensing flow.

Notice that both q''_{cond} and h_{cond} vary along the condenser tubes, and corresponding local thermodynamic equilibrium quality is given by

$$x_{e,cond,z} = x_{e,cond,in} - \int_0^z \frac{q''_{cond}(2\pi\ r_i)}{G_{cond}(\pi\ r_i^2)h_{fg}}dz\,. \tag{26}$$

Eq. (26) can be used to determine extents of upstream superheated region, $L_{sp,g}$, two-phase region, L_{tp}, and single-phase liquid region, $L_{sp,f}$, according to

$$\int_0^{L_{sp,g}} q''_{cond}(2\pi\ r_i)dz = G_{cond}(\pi\ r_i^2)c_{p,g}(T_{g,in} - T_{sat,in})\,, \tag{27}$$

$$\int_{L_{sp,g}}^{L_{sp,g}+L_{tp}} q''_{H}(2\pi\ r_i)dz = G_{cond}(\pi r_i^2)h_{fg}\,, \tag{28}$$

and

$$L_{sp,f} = L_{cond} - L_{tp} - L_{sp,g}\,. \tag{29}$$

Total condenser charge is the sum of charges of the three regions,

$$C_{cond} = C_{cond,sp,g} + C_{cond,tp} + C_{cond,sp,f}\,, \tag{30}$$

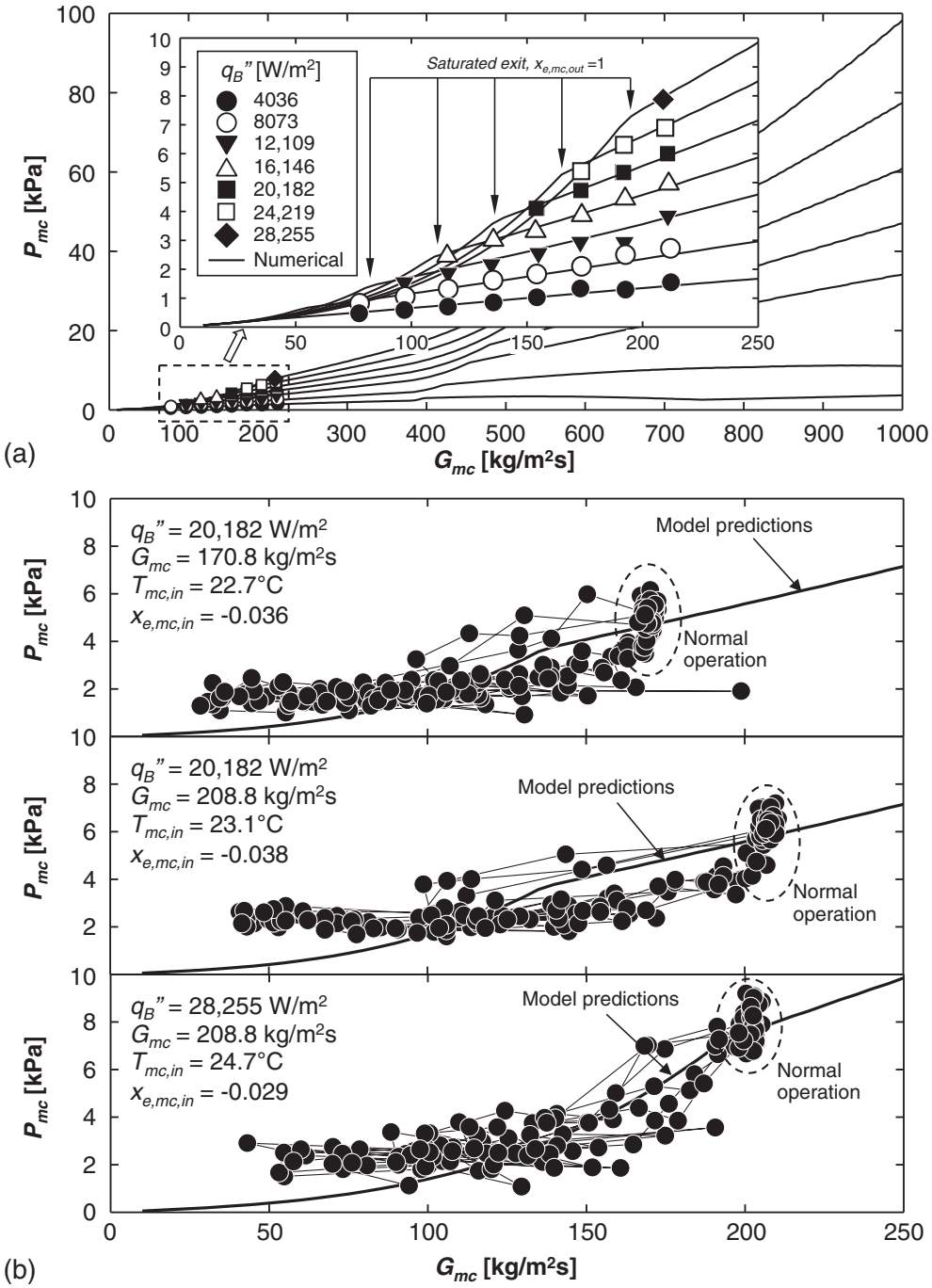

Fig. 14. Micro-channel ΔP_{mc} versus G_{mc} characteristics. (a) Characteristics for steady-state data achieved with PID control following CTI compared to model predictions. (b) Characteristics for transient CTI data for three sets of operating conditions compared to model predictions.

$$C_{cond,sp,g} = (\pi\ r_i^2)\int_0^{L_{sp,g}} \rho_g dz\,, \tag{31}$$

$$C_{cond,tp} = (\pi r_i^2)\int_{L_{sp,g}}^{L_{sp,g}+L_{tp}} \left(\rho_g \alpha_{cond,z} + \rho_f(1-\alpha_{cond,z})\right) dz\,, \tag{32}$$

and

$$C_{cond,sp,f} = (\pi r_i^2)\int_{L_{sp,g}+L_{tp}}^{L_{cond}} \rho_f dz. \tag{33}$$

Tables A.1 and A.2 provide different methods that were attempted to determine the condenser's void fraction, $\alpha_{cond,z}$, and condensation heat transfer coefficient, respectively, for calculation of C_{cond}.

6.3. Comparison of CTI charge model with experimental results

Excepting the reservoir, total fluid charge in the loop, C_{loop}, is estimated from measurement of level indicator installed in the reservoir, and is the sum of charges in four parts of the loop,

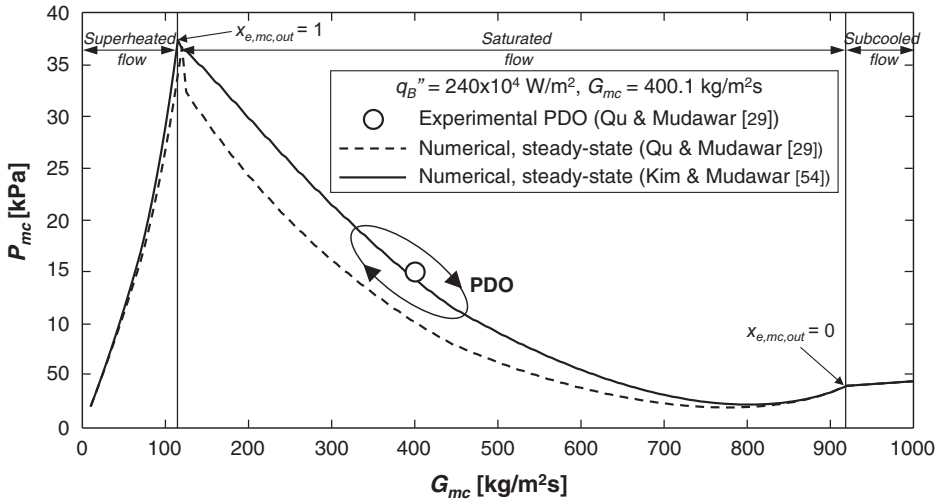

Fig. 15. Variation of micro-channel pressure drop versus mass velocity, including pressure drop oscillation (PDO) region for water data from Qu and Mudawar [29], and steady-sate predictions for same operating conditions according to Qu and Mudawar, and Kim and Mudawar [54].

Table A1
Void fraction relations attempted in prediction of onset of CTI. In this table $\alpha = \alpha_{cond,z}$, $x = x_{e,cond,z}$, $G = G_{cond}$, and $D_h = D_i$.

Basic form: $\alpha = \frac{1}{1+\left(\frac{1-x}{x}\right)\left(\frac{\rho_g}{\rho_f}\right)S}$

1. Homogeneous equilibrium model

HEM: $S = 1$

2. Slip-ratio based

Rigot (1973) [64]: $S = 2$

Ahrens (1980) [65], Thom (1983) [66]: $S = f(P.I.)$, $P.I. = \left(\frac{\mu_f}{\mu_g}\right)^{0.2}\left(\frac{\rho_g}{\rho_f}\right)$

$P.I.$	0.00116	0.0154	0.0375	0.0878	0.187	0.446	1.0
S	6.45	2.48	1.92	1.57	1.35	1.15	1.0

Zivi (1964) [58]: $S = \left(\frac{\rho_g}{\rho_f}\right)^{-1/3}$

Smith (1969) [67]: $S = 0.4 + (1-0.4)\left[\frac{\left(\frac{\rho_f}{\rho_g}\right)+0.4\left(\frac{1-x}{x}\right)}{1+0.4\left(\frac{1-x}{x}\right)}\right]^{1/2}$

3. X_{tt} based

Lockhart-Martinelli (1949) [68], Wallis (1969) [69], Domanski & Didion (1983) [70]:
$\alpha = \left(1+X_{tt}^{0.8}\right)^{-0.378}$ for $X_{tt} \leqslant 10$
$\alpha = 0.823 - 0.157 \ln X_{tt}$ for $X_{tt} > 10$
$X_{tt} = \left(\frac{\mu_f}{\mu_g}\right)^{0.1}\left(\frac{1-x}{x}\right)^{0.9}\left(\frac{\rho_g}{\rho_f}\right)^{0.5}$

Baroczy (1965) [71]: Liquid fraction, $\alpha_f = (1-\alpha)$

	X_{tt}										
$P.I.$	0.01	0.04	0.1	0.2	0.5	1	3	5	10	30	100
0.00002				0.0012	0.009	0.068	0.17	0.22	0.3	0.47	0.71
0.0001			0.0015	0.0054	0.030	0.104	0.23	0.29	0.38	0.57	0.79
0.0004		0.0022	0.0072	0.180	0.066	0.142	0.28	0.35	0.45	0.67	0.85
0.001	0.0018	0.0066	0.0170	0.0345	0.091	0.170	0.32	0.40	0.50	0.72	0.88
0.004	0.0043	0.0165	0.0370	0.0650	0.134	0.222	0.39	0.48	0.58	0.80	0.92
0.01	0.0050	0.0210	0.0475	0.0840	0.165	0.262	0.44	0.53	0.63	0.84	0.94
0.04	0.0056	0.0250	0.0590	0.1050	0.215	0.330	0.53	0.63	0.72	0.90	0.96
0.1	0.0058	0.0268	0.0640	0.1170	0.242	0.380	0.60	0.70	0.78	0.92	0.98
1.0	0.0060	0.0280	0.0720	0.1400	0.320	0.500	0.75	0.85	0.90	0.94	0.994

4. Mass velocity based

Premoli et al. (1970) [72]:
$S = 1 + F_1\left(\frac{y}{1+yF_2} - yF_2\right)^{1/2}$
$F_1 = 1.578\, Re_{fo}^{-0.19}\left(\frac{\rho_f}{\rho_g}\right)^{0.22}$, $F_2 = 0.0273\, We_{fo} Re_{fo}^{-0.51}\left(\frac{\rho_f}{\rho_g}\right)^{-0.08}$, $y = \frac{\beta_v}{1-\beta_v}$,
$We_{fo} = \frac{G^2 D_h}{\sigma \rho_f}$, $Re_{fo} = \frac{G D_h}{\mu_f}$, $\beta_v = \frac{1}{1+\left(\frac{1-x}{x}\right)\left(\frac{\rho_g}{\rho_f}\right)}$

Hughmark (1962) [73]:
$\alpha = \frac{K_H}{1+\left(\frac{1-x}{x}\right)\left(\frac{\rho_g}{\rho_f}\right)} = K_H \beta_v$
$Z = \frac{Re_z^{1/6} Fr^{1/8}}{y_L^{1/4}}$, $Re_z = \frac{D_h G}{\mu_f + \alpha(\mu_g - \mu_f)}$, $Fr = \frac{1}{g D_h}\left(\frac{Gx}{\beta_v \rho_g}\right)^2$,
$y_L = \frac{1}{1+\left(\frac{x}{1-x}\right)\frac{\rho_f}{\rho_g}} = 1 - \beta_v$

Z	1.3	1.5	2	3	4	5	6	8	10	15	20
K_H	0.185	0.225	0.325	0.49	0.605	0.675	0.72	0.767	0.78	0.808	0.83

Table A2
Empirical heat transfer correlations for saturated condensing flow attempted in prediction of onset of CTI. In this table $h_{tp} = h_{cond}$, $x = x_{e,cond,z}$, $G = G_{cond}$, and $D_h = D_i$.

Author(s)		Remarks
Akers & Rosson (1960) [74]	$h_{tp} = \left(\frac{k_f}{D_h}\right) 0.026 Pr_f^{1/3} \left\{ G\left[(1-x) + x\left(\frac{\rho_f}{\rho_g}\right)^{0.5}\right]\frac{D_h}{\mu_f}\right\}^{0.8}$ $Re_g \left(\frac{\mu_g}{\mu_f}\right)\left(\frac{\rho_f}{\rho_g}\right)^{0.5} > 20{,}000$, $Re_f > 5000$	Diameter: 19.05 mm Fluids: R12, propane
Cavallini & Zecchin (1974) [75]	$h_{tp} = \left(\frac{k_f}{D_h}\right) 0.05 Re_f^{0.8} Pr_f^{0.33}\left[1 + \left(\frac{\rho_f}{\rho_g}\right)^{0.5}\left(\frac{x}{1-x}\right)\right]^{0.8}$ $7000 \leqslant Re_{fo} \leqslant 53{,}000$	Fluids: R12, R22, R113
Shah (1979) [76]	$h_{tp} = \left(\frac{k_f}{D_h}\right) 0.023\, Re_{fo}^{0.8} Pr_f^{0.4}\left[(1-x)^{0.8} + \frac{3.8\, x^{0.76}(1-x)^{0.04}}{P_R^{0.38}}\right]$	Diameter: 7–40 mm Fluids: water, R11, R12, R22, R113, methanol, ethanol, benzene, toluene, trichloroethylene
Haraguchi et al. (1994) [77]	$h_{tp} = \left(\frac{k_f}{D_h}\right) 0.0152\left(1 + 0.6 Pr_f^{0.8}\right)\frac{\phi_g}{X_{tt}} Re_f^{0.77}$ $\phi_g = 1 + 0.5\left[\frac{G}{\sqrt{g\rho_g(\rho_f-\rho_g)D_h}}\right]^{0.75} X_{tt}^{0.35}$	Diameter: 8.4 mm Fluids: R22, R123, R134a
Dobson & Chato (1998) [78]	$h_{tp} = \left(\frac{k_f}{D_h}\right) 0.023 Re_f^{0.8} Pr_f^{0.4}\left(1 + \frac{2.22}{X_{tt}^{0.89}}\right)$	Diameter: 3.14–7.04 mm Fluids: R12, R22, R134a, R32/R125
Moser et al. (1998) [79]	$h_{tp} = \left(\frac{k_f}{D_h}\right)\frac{0.0994^{C_1} Re_f^{C_2} Re_{eq}^{1+0.875C_1} Pr_f^{0.815}}{(1.58\ln Re_{eq} - 3.28)\left(2.58\ln Re_{eq} + 13.7 Pr_f^{2/3} - 19.1\right)}$ $C_1 = 0.126\ \ Pr_f^{-0.448}$, $C_2 = -0.113\ \ Pr_f^{-0.563}$, $Re_{eq} = \phi_{fo,Friedel}^{8/7} Re_{fo}$, $\phi_{fo,Friedel}^2 = A_1 + \frac{3.24 A_2}{Fr^{0.045} We^{0.035}}$, $Fr = G^2/\left(g\, D_h\ \rho_{tp}^2\right)$, $We = \left(G^2 D_h\right)/\left(\rho_{tp}\sigma\right)$, $A_1 = (1-x)^2 + x^2\left(\frac{\rho_f}{\rho_g}\right)\left(\frac{f_{go}}{f_{fo}}\right)$, $A_2 = x^{0.78}(1-x)^{0.24}\left(\frac{\rho_f}{\rho_g}\right)^{0.91}\left(\frac{\mu_g}{\mu_f}\right)^{0.19}\left(1-\frac{\mu_g}{\mu_f}\right)^{0.70}$, $\rho_{tp} = \left(\frac{x}{\rho_g} + \frac{1-x}{\rho_f}\right)^{-1}$	Diameter: 3.14–20 mm Fluids: R11, R12, R125, R22, R134a, R410A
Shah (2009) [80]	Region 1: ($J_g \geqslant 0.98(Z+0.263)^{-0.62}$): $h_{tp} = h_I$ Region 2: ($J_g < 0.98(Z+0.263)^{-0.62}$): $h_{tp} = h_I$ for $Re_{go} < 35{,}000$ (horizontal flow) $h_{tp} = h_I + h_{NU}$ for $Re_{go} \geqslant 35{,}000$ $h_I = h_{sp,fo}\left(\frac{\mu_f}{14\ \mu_g}\right)^n \left[(1-x_e)^{0.8} + \frac{3.8\ x^{0.76}(1-x_e)^{0.04}}{P_R^{0.38}}\right]$ $h_{NU} = 1.32\, Re_f^{-1/3}\left[\frac{\rho_f(\rho_f-\rho_g)g\ k_f^3}{\mu_f^2}\right]^{1/3}$, $h_{sp,fo} = 0.023\ \ Re_{fo}^{0.8} Pr_f^{0.4}\frac{k_f}{D_h}$, $n = 0.0058 + 0.557 P_R$, $J_g = \frac{x\, G}{\left[g\ D_h \rho_g(\rho_f-\rho_g)\right]^{0.5}}$, $Z = \left(\frac{1}{x}-1\right)^{0.8} P_R^{0.4}$	Diameter: 2.0–49.0 mm Fluids: benzene, Dowtherm 209, ethanol, isobutene, methanol, propylene, propane, toluene, water, R11, R113, R12, R123, R125, R134a, R142b, R22, R32, R404, R410A, R502, R507. G: 4–820 kg/m^{2}s $68 < Re_{fo} < 85{,}000$ $0.0008 < P_R < 0.9$ $1 < \mathrm{Pr}_f < 18$
Bohdal et al. (2011) [81]	$h_{tp} = \left(\frac{k_f}{D_h}\right)\ 25.084\ \ Re_f^{0.258} Pr_f^{-0.495} P_R^{0.288}\left(\frac{x}{1-x}\right)^{0.266}$	Diameter: 0.31–3.30 mm Fluids: R134a, R404A
Kim & Mudawar (2012) [82]	For annular flow ($We^* \geqslant 7X_{tt}^{0.2}$): $\frac{h_{ann} D_h}{k_f} = 0.048 Re_f^{0.69} Pr_f^{0.34}\frac{\phi_g}{X_{tt}}$ For non-annular flow (Bubbly and slug) ($We^* < 7X_{tt}^{0.2}$): $\frac{h_{non-ann} D_h}{k_f} = \left[\left(0.048 Re_f^{0.69} \mathrm{Pr}_f^{0.34}\frac{\phi_g}{X_{tt}}\right)^2 + \left(3.2\times 10^{-7} Re_f^{-0.38} Su_{go}^{1.39}\right)^2\right]^{0.5}$ $We^* = 2.45\frac{Re_g^{0.64}}{Su_{go}^{0.3}\left(1+1.09 X_{tt}^{0.039}\right)^{0.4}}$ for $Re_f < 1250$ $We^* = 0.85\frac{Re_g^{0.79} X_{tt}^{0.157}}{Su_{go}^{0.3}\left(1+1.09 X_{tt}^{0.039}\right)^{0.4}}\left[\left(\frac{\mu_g}{\mu_f}\right)^2\left(\frac{\nu_g}{\nu_f}\right)\right]^{0.084}$ for $Re_f \geqslant 1250$ $Re_g = \frac{G\ x\ D_h}{\mu_g}$, $Re_{fo} = \frac{G\ D_h}{\mu_f}$, $Su_{go} = \frac{\rho_g \sigma D_h}{\mu_g^2}$ $X_{tt} = \left(\frac{\mu_f}{\mu_g}\right)^{0.1}\left(\frac{1-x}{x}\right)^{0.9}\left(\frac{\rho_g}{\rho_f}\right)^{0.5}$, $\phi_g^2 = 1 + C\, X + X^2$, $X^2 = \frac{(dP/dz)_f}{(dP/dz)_g}$ $-\left(\frac{dP}{dz}\right)_f = \frac{2 f_f \nu_f G^2 (1-x)^2}{D_h}$, $-\left(\frac{dP}{dz}\right)_g = \frac{2 f_g \nu_g G^2 x^2}{D_h}$, $f_k = 16 Re_k^{-1}$ for $Re_k < 2000$ $f_k = 0.079 Re_k^{-0.25}$ for $2000 \leqslant Re_k < 20{,}000$ $f_k = 0.046 Re_k^{-0.2}$ for $Re_k \geqslant 20{,}000$ (i) Turbulent-turbulent: $Re_f \geqslant 2000$, $Re_g \geqslant 2000$ $C = 0.39 Re_{fo}^{0.03} Su_{go}^{0.10}\left(\frac{\rho_f}{\rho_g}\right)^{0.35}$ (ii) Turbulent-laminar: $Re_f \geqslant 2000$, $Re_g < 2000$ $C = 8.7\times 10^{-4} Re_{fo}^{0.17} Su_{go}^{0.50}\left(\frac{\rho_f}{\rho_g}\right)^{0.14}$ (iii) Laminar-turbulent: $Re_f < 2000$, $Re_g \geqslant 2000$ $C = 0.0015 Re_{fo}^{0.59} Su_{go}^{0.19}\left(\frac{\rho_f}{\rho_g}\right)^{0.36}$ (iv) Laminar-laminar: $Re_f \geqslant 2000$,$Re_g < 2000$ $C = 3.5\times 10^{-5} Re_{fo}^{0.44} Su_{go}^{0.50}\left(\frac{\rho_f}{\rho_g}\right)^{0.48}$	Diameter: 0.424–6.22 mm Fluids: R12, R123, R1234yf, R1234ze(E), R134a, R22, R236fa, R245fa, R32, R404A, R410A, R600a, FC72, methane, and CO_2 G: 53–1403 kg/m^2 s $276 < Re_{fo} < 89{,}798$ $0 < Re_f < 79{,}202$ $0 < Re_g < 247{,}740$ $0 \leqslant x \leqslant 1$ $0.04 \leqslant P_R \leqslant 0.91$

micro-channel test module, C_{mc}, loop components between test module and condenser, $C_{mc\text{-}cond}$, condenser itself, C_{cond}, and loop components between condenser and test module, $C_{cond\text{-}mc}$.

$$C_{loop} = C_{mc} + C_{mc-cond} + C_{cond} + C_{cond-mc} . \quad (34)$$

The individual charges are calculated using the methodology outlined in the previous sections and Appendix A, of which condenser charge is found to vary most with changes in operating conditions. This required special care in condenser calculations using nine different correlations for void fraction, Table A.1, and 18 correlations for condensation heat transfer coefficient, Table A.2.

Predicted loop charge under CTI ($C_{loop} = C_{loop,CTI,pred}$) is compared to 69 charge measurements, calculated according to

$$C_{loop,CTI,\exp} = C_{total} - C_{res} , \quad (35)$$

where C_{total} is total mass of R134a in the entire system. The onset of CTI for both with and without PID control could be identified using two different criteria, mild and sharp, as discussed in Section 3; the one based on sharp charge drop (identified by minimum C_{loop}) is used to model onset of CTI.

Fig. 16 compares predicted and measured values of loop charge at CTI. Accuracy of predictions using different combinations of

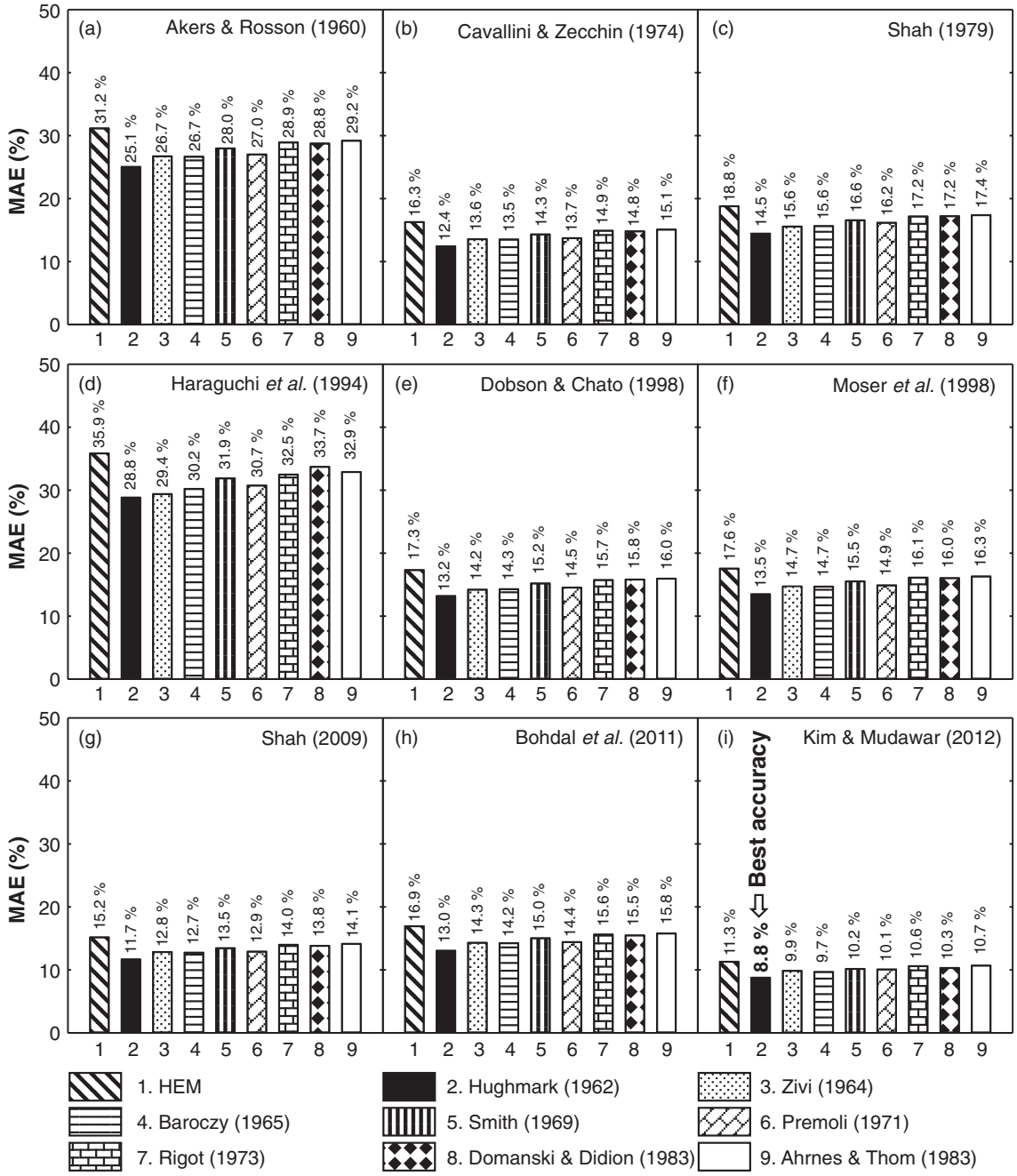

Fig. 16. MAE achieved using different condensation heat transfer coefficient and void fraction predictive methods to calculate loop charge, C_{loop}, at CTI initiation based on criterion of minimum loop charge. The heat transfer coefficient is calculated using correlations by (a) Akers and Rosson [74], (b) Cavallini and Zecchin [75], (c) Shah [76], (d) Haraguchi et al. [77], (e) Dobson and Chato [78], (f) Moser et al. [79], (g) Shah [80], (h) Bohdal et al. [81], and (i) Kim and Mudawar [82]. The void faction calculations are based on (1) Homogeneous Equilibrium Model (HEM), (2) Hughmark [73], (3) Zivi [58], (4) Baroczy [71], (5) Smith [67], (6) Premoli [72], (7) Rigot [64], (8) Domanski and Didion [70], and (9) Ahrnes [65] and Thom [66].

condensation correlations is assessed using mean absolute error (MAE), which is expressed as

$$MAE\,(\%) = \frac{1}{N}\sum\left[\frac{\left|C_{loop,CTI,pred} - C_{loop,CTI,\exp}\right|}{C_{loop,CTI,\exp}} \times 100\right]. \quad (36)$$

Overall, as shown in Fig. 16(i), smallest MAE of 8.8% is achieved using Kim and Mudawar's [82] correlation for condensation heat transfer coefficient combined with Hughmark's [73] correlation for void fraction. It is noted that MAE is far more sensitive to choice of heat transfer correlation than to void fraction. However, the same combination underpredicts C_{loop} with a higher MAE of 21.7% when using mild mass velocity drop as criterion for onset of CTI, which can be explained by the mild condition occurring ahead of actual onset of CTI initiated by lack of loop charge.

Fig. 17(a) shows detailed comparison of predicted and measured CTI loop charge using the combined correlations of Kim and Mudawar, and Hughmark. Shown are all predictions falling well within ±30% of measurements. Fig. 17(b) shows C_{cond} and $C_{cond\text{-}mc}$ contribute the most to C_{loop}, which can be explained by comparatively much smaller fluid volume in the micro-channel module compared to the condenser, and reinforces the rationale for careful assessment of condenser contribution when calculating MAE for C_{loop} at CTI.

7. Conclusions

This study investigates two-phase flow instabilities in a micro-channel heat sink module inserted in a pumped R134a loop. A dominant charge transition instability (CTI) is clearly identified as precipitating appreciable oscillations in micro-channel module's mass velocity and pressure drop. The study also discusses how PID control could be used to suppress CTI. A detailed analytical model is presented to predict onset of CTI when using PID control. Also discussed are differences in cooling system responses resulting

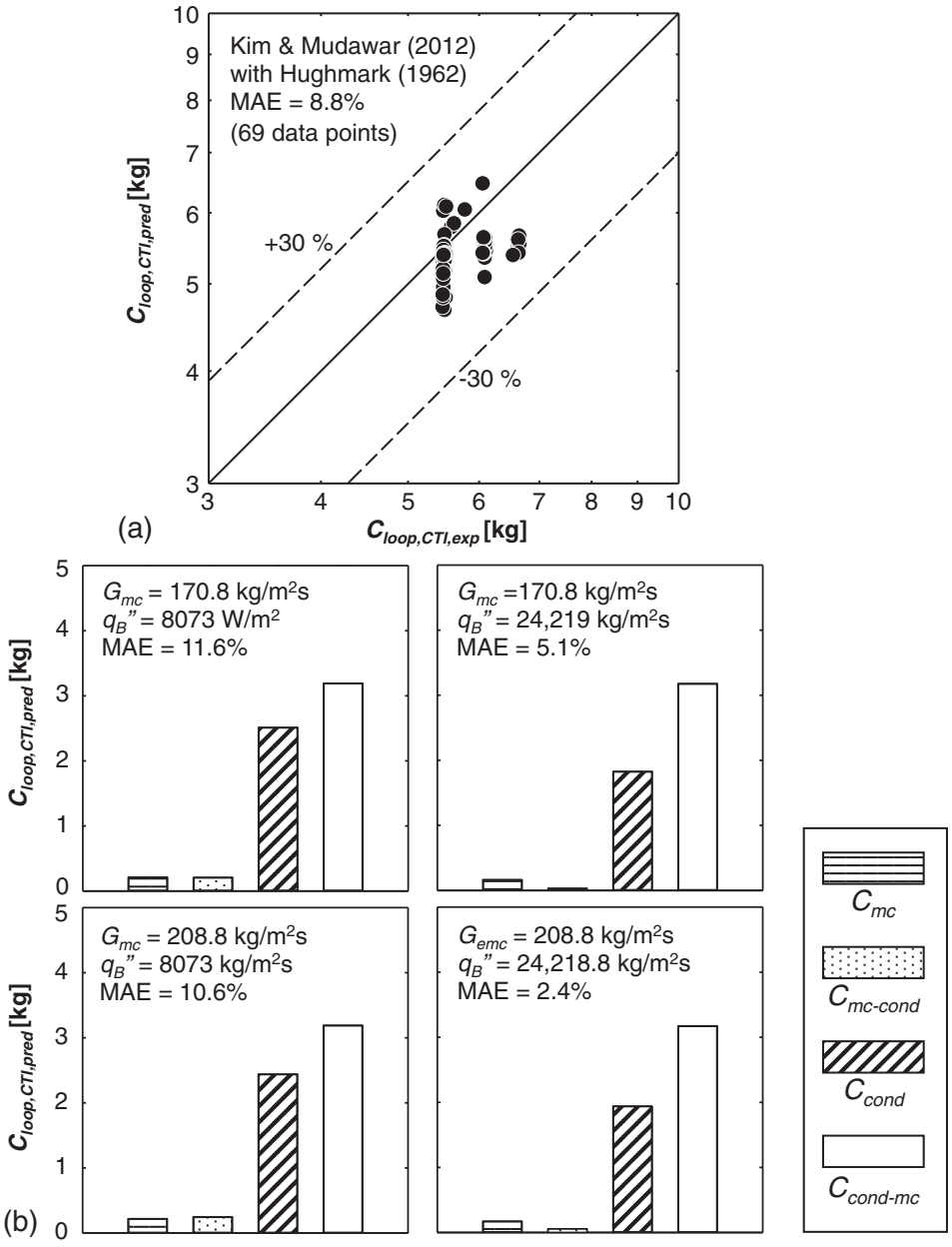

Fig. 17. Prediction of onset of CTI using correlations for condensation heat transfer coefficient by Kim and Mudawar [82] and void fraction by Hughmark [73]. (a) Comparison of predicted and measured loop charge at CTI. (b) Contributions of loop component charges to C_{loop}, calculated using correlations from (a) for different operating conditions.

from CTI, parallel channel instability (PCI), and pressure drop oscillation (PDO). Following are key conclusions from the study:

(1) Without PID control, CTI occurs in response to heat addition in the micro-channel heat sink, and is manifest by increased vapor generation in the loop increasing system pressure, forcing charge transition from loop to reservoir. The onset of CTI is associated with synchronized periodic oscillations in mass flow rate, micro-channel inlet and outlet pressures, condenser inlet and outlet pressures, and reservoir pressure.
(2) PID control can suppress CTI by increasing reservoir pressure. However, specific criteria for PID set pressure, dictated mostly by ambient temperature, must be met to ensure successful suppression and return to normal steady-state operation.
(3) CTI can increase heat sink temperature by up to 30 °C before being suppressed by PID control system. However, PCI also occurs within individual CTI oscillation cycles, taking the form of comparatively small amplitude, high frequency oscillations. But maximum rise in heat sink temperature with PCI is only 5 °C, which proves dominance of CTI compared to PCI.
(4) The mechanisms of CTI and PDO are fundamentally different in that ensuing fluctuations in micro-channel heat sink mass velocity and pressure drop are synchronized for the former, but out of phase for the latter. Additionally, CTI occurs in the positive slope region of the heat sink's pressure drop versus mass velocity characteristics, while PDO occurs in the negative slope region.
(5) Because of comparatively much smaller fluid volume in the micro-channel module compared to the condenser, most of the loop charge (minus reservoir) is concentrated in the condenser as well as loop components between condenser and heat sink. Therefore, when using PID control, the condenser plays a major role in determining overall system stability.
(6) An analytical model, which includes detailed calculation of fluid charges in different parts of the system with PID control, is used to predict CTI commencement once total loop charge (minus reservoir) falls below a low threshold required for normal operation. Given high sensitivity of CTI to condenser operation, analysis is presented that includes evaluation of several alternative empirical formulations for condenser thermal performance. Overall, best predictions of minimum loop charge (MAE = 8.8%) are achieved with a condensation heat transfer coefficient correlation by Kim and Mudawar [82], combined with a void fraction correlation by Hughmark [73].
(7) Given the importance of CTI suppression to overall cooling system performance, it is recommended that future work be performed to monitor detailed vapor generation everywhere in a cooling loop, as well as explore alternative PID controls, including provision for pneumatic adjustment of reservoir pressure. For industrial use, loop charge signals can be used with the analytical model presented in this study for early detection as well as prevention of instability.

Declaration of Competing Interest

The authors declared that there is no conflict of interest.

Acknowledgements

The authors are grateful for support from Center of Excellence for Integrated Thermal Management of Aerospace Vehicles (CITMAV) under grant No. F. 90000277.02.018, and National Aeronautics and Space Administration (NASA) under grant No. NNX13AB01G.

Appendix A

A.1 Condenser thermal resistances

Fig. A1(a) shows both longitudinal and cross-sectional views of the finned-tube condenser employed in the present study, including definitions for key geometrical parameters. Fig. A1(b) provides an equivalent thermal circuit for a single tube, along with definition of resistance parameters, used to calculate local condenser heat transfer rate for a single unit cell. The total resistance from internal R134a flow to ambient air per unit tube length Δz is expressed as

$$R_{total} = R_{cond} + R_w + R_{\text{equiv}}\,, \tag{A41}$$

where R_{cond}, R_w, and R_{equiv} are, respectively, resistances associated with internal condensing flow, tube wall, and finned outer surface. The first two resistances can be expressed as

$$R_{cond} = \frac{1}{h_{cond}\ (2\pi\, r_i\,)\Delta\ z} \tag{A2}$$

and

$$R_w = \frac{\ln(r_o/r_i)}{2\ \pi\ k_w\ \Delta z}\,, \tag{A3}$$

where h_{cond} and k_w are the condensation heat transfer coefficient and tube thermal conductivity, respectively.

Equivalent resistance for the outer surface is calculated according to

$$\frac{1}{R_{\text{equiv}}} = \frac{1}{R_{fin}} + \frac{1}{R_{unfin}}\,, \tag{A4}$$

where R_{fin} and R_{unfin} are resistances of fin and bare outer surface, based on mean outer airside heat transfer coefficient, h_{air}, which are expressed, respectively, by

$$R_{fin} = \frac{1}{\bar{h}_{air} N_{fin}\, \eta_{fin} A_{fin}} \tag{A5}$$

and

$$R_{unfin} = \frac{1}{\bar{h}_{air} A_{unfin}}\,. \tag{A6}$$

In Eq. (A5), N_{fin} is number of fins per unit length, and η_{fin}, A_{fin}, and A_{unfin} are fin efficiency, fin surface area, and bare surface area, which are expressed, respectively, as

$$\eta_{fin} = \frac{\tanh\ \ (m_{fin}\ r_o\ \ \phi)}{m_{fin}\, r_o\ \ \ \phi}\,, \tag{A7}$$

$$A_{fin} = \left(8\ X_T\ X_L - 2\pi\ r_o^2\right), \tag{A8}$$

and

$$A_{unfin} = N_{fin} 2\pi r_o \left(p_{fin} - t_{fin}\right). \tag{A9}$$

The fin parameters in Eq. (A7) are calculated according to [59]

$$m_{fin} = \sqrt{\frac{2\ \bar{h}_{air}}{k_{fin}\, t_{fin}}} \tag{A10a}$$

and

$$\phi = \left(\frac{r_{equiv}}{r_o} - 1\right)\left(1 + 0.35\ \ln\left(\frac{r_{equiv}}{r_o}\right)\right), \tag{A10b}$$

where r_{equiv} is equivalent radius, which is expressed as [60,61]

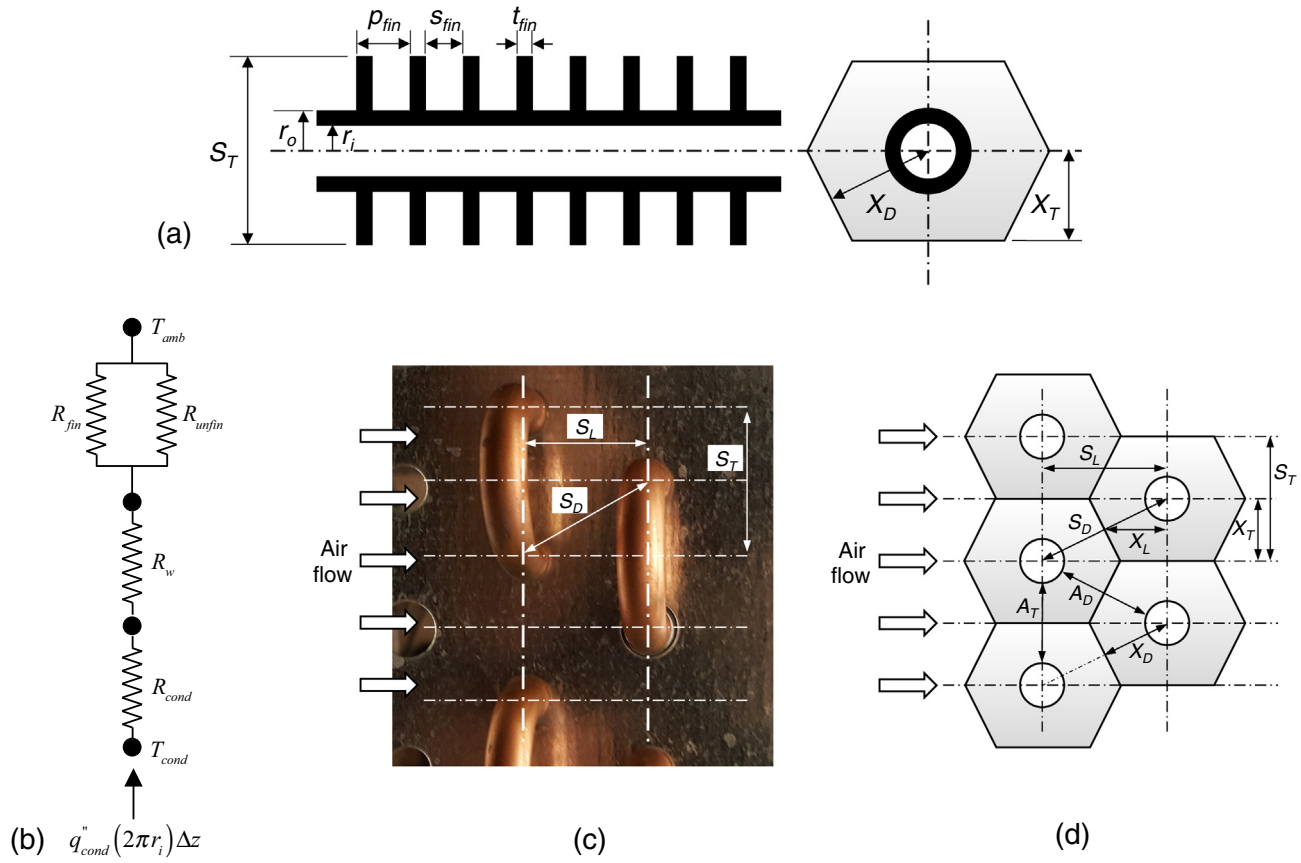

Fig. A1. (a) Longitudinal and cross-sectional views of single unit of finned condenser tube. (b) Equivalent thermal circuit between condensing fluid and ambient air. (c) End view of condenser tubes. (d) Schematic diagram of airside fin arrangement.

$$\frac{r_{equiv}}{r_o} = 1.27\frac{X_T}{r_o}\left(\frac{X_D}{X_T} - 0.3\right)^{1/2} = 1.27\frac{S_T}{2\ r_o}\sqrt{\frac{\left(S_L^2 + (S_T/2)^2\right)^{1/2}}{S_T} - 0.3}, \quad (N_{row} \geqslant 2) \tag{A11}$$

A.2 Condenser average airside heat transfer coefficient

Figs. A1(c) and (d) are used as guides for condenser's airside geometrical parameters. The Colburn j factor, $Nu/(RePr^{1/3})$, for fin-and-tube heat exchanger with staggered tubes is determined using following correlations, depending on number of tube rows, N_{row}, [62],

$$j_3 = St_{D_o}Pr_{air}^{2/3} = 0.163\,Re_{D_o}^{-0.369}\left(\frac{S_T}{S_L}\right)^{0.106}\left(\frac{s_{fin}}{D_o}\right)^{0.0138}\left(\frac{S_T}{D_o}\right)^{0.13} \quad \text{for } N_{row} \geqslant 3 \tag{A12}$$

and

$$\frac{j_{N=1,2}}{j_3} = 1.043\left[Re_{D_o}^{-0.14}\left(\frac{S_T}{S_L}\right)^{-0.564}\left(\frac{s_{fin}}{D_o}\right)^{-0.123}\left(\frac{S_T}{D_o}\right)^{1.17}\right]^{(3-N_{row})} \quad \text{for } N_{row} = 1,2 \tag{A13}$$

where

$$St_{D_o} = \frac{\overline{Nu}_{D_o}}{Re_{D_o}\ Pr_{air}} \tag{A14}$$

$$\overline{Nu}_{Do} = \frac{\bar{h}_{air}\ D_o}{k_{air}}, \tag{A15}$$

and

$$Re_{D_o} = \frac{\dot{m}_{air}\ D_o}{\mu_{air}\ A_{air,\min}}. \tag{A16}$$

In Eq. (A16), $A_{air,\min}$ is the smaller of flow areas in traverse plane,

$$A_T = \frac{n\ L_{cond,1p}\ s_{fin}}{s_{fin} + t_{fin}}(S_T - D_o), \tag{A17}$$

and in diagonal plane,

$$A_D = \frac{2\ n\ L_{cond,1p} s_{fin}}{s_{fin} + t_{fin}}(S_D - D_o), \tag{A18}$$

where

$$S_D = \sqrt{\left(\frac{S_T}{2}\right)^2 + S_L^2}, \tag{A19}$$

n is number of tubes in one row (or one plane), and $L_{cond,1}$ length of single condenser tube pass.

The overall airside heat transfer coefficient is determined (based on N_{row} = 1,2 for present condenser) as

$$\bar{h}_{air} = \frac{k_{air}}{D_o}Re_{D_o}\ Pr_{air}^{1/3}j_3 \times 1.043\left[Re_{D_o}^{-0.14}\left(\frac{S_T}{S_L}\right)^{-0.564}\left(\frac{s_{fin}}{D_o}\right)^{-0.123}\left(\frac{S_T}{D_o}\right)^{1.17}\right]^{(3-N_{row})}. \tag{A20}$$

A.3 Condensation pressure drop and heat transfer coefficient

Total pressure drop across the condenser, ΔP_{cond}, is expressed as

$$\Delta P_{cond} = \Delta P_c + \Delta P_{sp,g} + \left(\Delta P_{tp,A} + \Delta P_{tp,F}\right) + \Delta P_{sp,f} + \Delta P_e\,, \tag{A21}$$

where ΔP_c, $\Delta P_{sp,g}$, $\Delta P_{tp,A}$, $\Delta P_{tp,F}$, $\Delta P_{sp,f}$, and ΔP_e are, respectively, pressure drop components associated with inlet contraction, upstream superheated single-phase vapor, two-phase acceleration (negative for condensation), two-phase friction, single-phase liquid, and outlet expansion. Given long condenser tubing length, inlet contraction and outlet expansion components are comparatively negligible. And, pressure drops in the single-phase superheated vapor and subcooled liquid regions are expressed, respectively, as

$$\Delta P_{sp,k} = \frac{2 f_{ko} G_{cond}^2 \; L_{sp,k} \, v_{sp,k}}{D_i} \tag{A22}$$

with

$$f_{ko} = \frac{c}{Re_{ko}^n} = \frac{c}{\left(\frac{G_{cond} D_i}{\mu_k}\right)^n}\,, \tag{A23}$$

where $k = g$ for vapor and $k = f$ for liquid. The constants c and n in Eq. (A23) as given by [63]

$$c = 16, n = 1 \quad \text{for} \quad Re_{ko} < 2{,}000 \tag{A24}$$

$$c = 0.079, n = 0.25 \quad \text{for} \quad 2{,}000 \leqslant Re_{ko} < 2 \times 10^4, \tag{A25}$$

$$c = 0.046, n = 0.20 \quad \text{for} \quad Re_{ko} \geqslant 2 \times 10^4 \tag{A26}$$

The accelerational pressure gradient in the two-phase flow region is expressed as

$$-\left(\frac{dP}{dz}\right)_A = G_{cond}^2 \frac{d}{dz}\left[v_g \frac{x_{e,cond,z}^2}{\alpha_{cond,z}} + v_f \frac{\left(1 - x_{e,cond,z}\right)^2}{\left(1 - \alpha_{cond,z}\right)^2}\right]$$

$$= G^2 \frac{dx_{e,cond,z}}{dz}\left\{2\left[v_g \frac{x_{e,cond,z}}{\alpha_{cond,z}} - v_f \frac{1 - x_{e,cond,z}}{1 - \alpha_{cond,z}}\right]\right.$$

$$\left. - \left[v_g \frac{x_{e,cond,z}^2}{\alpha_{cond,z}^2} - v_f \frac{\left(1 - x_{e,cond,z}\right)^2}{\left(1 - \alpha_{cond,z}\right)^2}\right] \frac{d\alpha_{cond,z}}{dx_{e,cond,z}}\right\}\,. \tag{A27}$$

Tables A.1 and A.2 provide different predictive methods for void fraction, $\alpha_{cond,z}$, and condensation heat transfer coefficient that are attempted in the present study for calculation of condenser charge.

The frictional pressure gradient for condensation is expressed as

$$\left(\frac{dP}{dz}\right)_F = \left(\frac{dP}{dz}\right)_{fo} \phi_{fo}^2\,, \tag{A28}$$

where

$$\left(\frac{dP}{dz}\right)_{fo} = \frac{2 f_{fo} G_{cond}^2 \, v_{sp,f} \; \Delta z}{D_i}\,. \tag{A29}$$

The friction multiplier ϕ_{fo}^2 in Eq. (A28) is expressed, for annular flow ($j_g* \geqslant 2.5$) [83], as

$$\phi_{fo}^2 = \left(1 - x_{e,cond,z}\right)^2 + x_{e,cond,z}^2 \left(\frac{v_g}{v_f}\right)\left(\frac{f_{go}}{f_{fo}}\right) + \ldots$$

$$+ 1.262\, x_{e,cond,z}^{0.6978} \left(\frac{v_g}{v_f}\right)^{0.3278} \left(\frac{\mu_g}{\mu_f}\right)^{-1.181} \left(1 - \frac{\mu_g}{\mu_f}\right)^{3.477} We_{tp}^{-0.1458}\,, \tag{A30a}$$

and, for other flow regimes ($j_g* < 2.5$) [84],

$$\phi_{fo}^2 = \left(1 - x_{e,cond,z}\right)^2 + x_{e,cond}^2 \left(\frac{v_g}{v_f}\right)\left(\frac{f_{go}}{f_{fo}}\right)$$

$$+ \ldots + 3.24\, x_{e,cond,z}^{0.78} \left(1 - x_e\right)^{0.224} \left(\frac{v_g}{v_f}\right)^{0.91} \left(\frac{\mu_g}{\mu_f}\right)^{0.19} \left(1 - \frac{\mu_g}{\mu_f}\right)^{0.7}$$

$$\times \, Fr_{tp}^{-0.045} \, We_{tp}^{-0.035}\,, \tag{A30b}$$

where

$$j_g* = \frac{G_{cond} \; x_{e,cond,z}}{\rho_g} \sqrt{\frac{\rho_g}{\left(\rho_f - \rho_g\right) g \; D_i}}\,, \tag{A31}$$

$$Fr_{tp} = \frac{G_{cond}^2}{g \; D_i \; \rho_H^2}\,, \tag{A32}$$

$$We_{tp} = \frac{G_{cond}^2 D}{\rho_H \sigma}\,, \tag{A33}$$

and

$$\rho_H = \frac{1}{x_{e,cond,z} v_g + \left(1 - x_{e,cond,z}\right) v_f}\,. \tag{A34}$$

Both wall heat flux and wall temperature change along the flow direction inside the condenser tube, so neither constant heat flux nor constant temperature boundary conditions are used for the single-phase vapor and liquid regions. Instead, an asymptotic solution for Nusselt-Graetz problem is used for laminar conditions [85], where heat transfer coefficient is given by

$$h_{sp,k,lam} = \frac{4.364 + Nu_w}{1 + Nu_w / 3.657}\left(\frac{k_k}{D_i}\right)\,, \tag{A35}$$

The wall Nusselt number, Nu_w, is defined bywhere

$$Nu_w = \frac{U_w \; D_i}{k_k}\,, \tag{A36}$$

and

$$\frac{1}{U_w (2\pi \; D_i \, \Delta z)} = \frac{1}{\eta_{air} \; \bar{h}_{air} \; A_{air,\Delta z}} + \frac{ln \; (D_o / D_i)}{2 \; \pi \;\; k_w \; \Delta z}\,, \tag{A37}$$

The first and second terms in Eq. (A37) are the air-side convection resistance and tube wall conduction resistance, respectively.

For turbulent single-phase vapor and liquid regions, the Dittus-Boelter equation is used,

$$h_{sp,k,turb} = 0.023 Re_{sp,k}^{0.8} Pr_k^{0.3} \frac{k_k}{D_i}\,. \tag{A38}$$

Appendix B. Supplementary material

Supplementary data to this article can be found online at https://doi.org/10.1016/j.ijheatmasstransfer.2019.05.077.

References

[1] I. Mudawar, Assessment of high-heat-flux thermal management schemes, IEEE Trans. - CPMT 24 (2001) 122–141.
[2] I. Mudawar, Two-phase micro-channel heat sinks: theory, applications and limitations, J. Electron. Packag. 133 (2011) 041002–41012.
[3] I. Mudawar, Recent advances in high-flux, two-phase thermal management, J. Therm. Sci. Eng. Appl. 5 (2013) 021012.
[4] T.J. LaClair, I. Mudawar, Thermal transients in a capillary evaporator prior to the initiation of boiling, Int. J. Heat Mass Transf. 43 (2000) 3937–3952.
[5] T.J. LaClair, I. Mudawar, Theoretical model for fast bubble growth in small channels with reference to startup of capillary pumped loops used in spacecraft thermal management systems, Int. J. Heat Mass Transf. 52 (2009) 716–723.

[6] I. Mudawar, T.M. Anderson, Parametric investigation into the effects of pressure, subcooling, surface augmentation and choice of coolant on pool boiling in the design of cooling systems for high-power density chips, J. Electron. Packag. 112 (1990) 375–382.
[7] T.H. Lyu, I. Mudawar, Determination of wave-induced fluctuations of wall temperature and convective heat transfer coefficient in the heating of a turbulent falling liquid film, Int. J. Heat Mass Transf. 34 (1991) 2521–2534.
[8] I. Mudawar, R.A. Houpt, Mass and momentum transport in smooth falling liquid films laminarized at relatively high Reynolds numbers, Int. J. Heat Mass Transf. 36 (1993) 3437–3448.
[9] C.O. Gersey, I. Mudawar, Effects of heater length and orientation on the trigger mechanism for near-saturated flow boiling CHF - I. Photographic and statistical characterization of the near-wall interfacial features, Int. J. Heat Mass Transf. 38 (1995) 629–642.
[10] C.O. Gersey, I. Mudawar, Effects of heater length and orientation on the trigger mechanism for near-saturated flow boiling CHF - II. CHF model, Int. J. Heat Mass Transf. 38 (1995) 643–654.
[11] J.C. Sturgis, I. Mudawar, Critical heat flux in a long, rectangular channel subjected to one-sided heating - II. Analysis of CHF data, Int. J. Heat Mass Transf. 42 (1999) 1849–1862.
[12] D.D. Hall, I. Mudawar, Ultra-high critical heat flux (CHF) for subcooled water flow boiling - II. High-CHF database and design parameters, Int. J. Heat Mass Transf. 42 (1990) 1429–1456.
[13] W. Qu, I. Mudawar, S.-Y. Lee, S.T. Wereley, Experimental and computational investigation of flow development and pressure drop in a rectangular micro-channel, J. Electron. Packag. 128 (2006) 1–9.
[14] S. Mukherjee, I. Mudawar, Smart pumpless loop for micro-channel electronic cooling using flat and enhanced surfaces, IEEE Trans. – CPMT 26 (2003) 99–109.
[15] M. Monde, T. Inoue, Critical heat flux in saturated forced convective boiling on a heated disk with multiple impinging jets, J. Heat Transf. 113 (1991) 722–727.
[16] M.E. Johns, I. Mudawar, An ultra-high power two-phase jet-impingement avionic clamshell module, J. Electron. Packag. 118 (1996) 264–270.
[17] W.P. Klinzing, J.C. Rozzi, I. Mudawar, Film and transition boiling correlations for quenching of hot surfaces with water sprays, J. Heat Treat. 9 (1992) 91–103.
[18] L. Lin, R. Ponnappan, Heat transfer characteristics of spray cooling in a closed loop, Int. J. Heat Mass Transf. 46 (2003) 3737–3746.
[19] M. Visaria, I. Mudawar, Application of two-phase spray cooling for thermal management of electronic devices, IEEE Trans. – CPMT 32 (2009) 784–793.
[20] M.K. Sung, I. Mudawar, Single-phase and two-phase heat transfer characteristics of low temperature hybrid micro-channel/micro-jet impingement cooling module, Int. J. Heat Mass Transf. 51 (2008) 3882–3895.
[21] M.K. Sung, I. Mudawar, Single-phase hybrid micro-channel/jet impingement cooling, Int. J. Heat Mass Transf. 51 (2008) 4342–4352.
[22] S.H. Lee, I. Mudawar, M.M. Hasan, Thermal analysis of hybrid single-phase, two-phase and heat pump thermal control system (TCS) for future spacecraft, Appl. Therm. Eng. 100 (2016) 190–214.
[23] H. Zhang, I. Mudawar, M.M. Hasan, Experimental assessment of the effects of body force, surface tension force, and inertia on flow boiling CHF, Int. J. Heat Mass Transf. 45 (2002) 4079–4095.
[24] H. Zhang, I. Mudawar, M.M. Hasan, Experimental and theoretical study of orientation effects on flow boiling CHF, Int. J. Heat Mass Transf. 45 (2002) 4463–4478.
[25] H. Zhang, I. Mudawar, M.M. Hasan, Flow boiling CHF in microgravity, Int. J. Heat Mass Transf. 48 (2005) 3107–3118.
[26] C. Konishi, I. Mudawar, M.M. Hasan, Investigation of the influence of orientation on critical heat flux for flow boiling with two-phase inlet, Int. J. Heat Mass Transf. 61 (2013) 176–190.
[27] H. Lee, I. Mudawar, M.M. Hasan, Experimental and theoretical investigation of annular flow condensation in microgravity, Int. J. Heat Mass Transf. 61 (2013) 293–309.
[28] J. Lee, I. Mudawar, Critical heat flux for subcooled flow boiling in micro-channel heat sinks, Int. J. Heat Mass Transf. 52 (2009) 3341–3352.
[29] W. Qu, I. Mudawar, Measurement and prediction of pressure drop in two-phase micro-channel heat sinks, Int. J. Heat Mass Transf. 46 (2003) 2737–2753.
[30] G. Wang, P. Cheng, A.E. Bergles, Effects of inlet/outlet configurations on flow boiling instability in parallel microchannels, Int. J. Heat Mass Transf. 51 (2008) 2267–2281.
[31] A. Koşar, C.J. Kuo, Y. Peles, Suppression of boiling flow oscillations in parallel microchannels by inlet restrictors, J. Heat Transf. 128 (2005) 251–260.
[32] S. Lee, I. Mudawar, Transient characteristics of flow boiling in large micro-channel heat exchangers, Int. J. Heat Mass Transf. 103 (2016) 186–202.
[33] S. Lee, V.S. Devahdhanush, I. Mudawar, Frequency analysis of pressure oscillations in large length-to-diameter two-phase micro-channel heat sinks, Int. J. Heat Mass Transf. 116 (2018) 273–291.
[34] S. Lee, V.S. Devahdhanush, I. Mudawar, Investigation of subcooled and saturated boiling heat transfer mechanisms, instabilities, and transient flow regime maps for large length-to-diameter ratio micro-channel heat sinks, Int. J. Heat Mass Transf. 123 (2018) 172–191.
[35] J.S. Maulbetsch, P. Griffith, A study of system-induced instabilities in forced-convection flows with subcooled boiling, Tech. Report No. 5382-35, Dept. of Mechanical Engineering, Massachusetts Institute of Technology, Cambridge, MA, 1965.
[36] M. Ozawa, K. Akagawa, T. Sakaguchi, Flow instabilities in parallel-channel flow systems of gas-liquid two-phase mixtures, Int. J. Multiphase Flow 15 (1989) 639–657.
[37] T. Zhang, T. Tong, J.-Y. Chang, Y. Peles, R. Prasher, M.K. Jensen, J.T. Wen, P. Phelan, Ledinegg instability in microchannels, Int. J. Heat Mass Transf. 52 (2009) 5661–5674.
[38] P. Saha, M. Ishii, N. Zuber, An experimental investigation of the thermally induced flow oscillations in two-phase systems, J. Heat Transf. 98 (1976) 616–622.
[39] H.C. Ünal, The period of density-wave oscillations in forced convection steam generator tubes, Int. J. Heat Mass Transf. 25 (1982) 419–421.
[40] K.H. Chang, C. Pan, Two-phase flow instability for boiling in a microchannel heat sink, Int. J. Heat Mass Transf. 50 (2007) 2078–2088.
[41] S. Lee, I. Mudawar, Investigation of flow boiling in large micro-channel heat exchangers in a refrigeration loop for space applications, Int. J. Heat Mass Transf. 97 (2016) 110–129.
[42] S. Lee, I. Mudawar, Thermal and thermodynamic performance, and pressure oscillations of refrigeration loop employing large micro-channel evaporators, Int. J. Heat Mass Transf. 103 (2016) 1313–1326.
[43] S. Lee, V.S. Devahdhanush, I. Mudawar, Pressure drop characteristics of large length-to-diameter two-phase micro-channel heat sinks, Int. J. Heat Mass Transf. 115 (2017) 1258–1275.
[44] L.E. O'Neill, I. Mudawar, M.M. Hasan, H.K. Nahra, R. Balasubramaniam, N.R. Hall, A. Lokey, J.R. Mackey, Experimental investigation into the impact of density wave oscillations on flow boiling system dynamic behavior and stability, Int. J. Heat Mass Transf. 120 (2018) 144–166.
[45] L.E. O'Neill, I. Mudawar, Mechanistic model to predict frequency and amplitude of Density Wave Oscillations in vertical upflow boiling, Int. J. Heat Mass Transf. 123 (2018) 143–171.
[46] L.E. O'Neill, I. Mudawar, M.M. Hasan, H.K. Nahra, R. Balasubramaniam, J.R. Mackey, Experimental investigation of frequency and amplitude of density wave oscillations in vertical upflow boiling, Int. J. Heat Mass Transf. 125 (2018) 1240–1263.
[47] L.E. O'Neill, I. Mudawar, M.M. Hasan, H.K. Nahra, R. Balasubramaniam, J.R. Mackey, Flow condensation pressure oscillations at different orientations, Int. J. Heat Mass Transf. 127 (2018) 784–809.
[48] T. Zhang, Y. Peles, J.T. Wen, T. Tong, J.-Y. Chang, R. Prasher, M.K. Jensen, Analysis and active control of pressure-drop flow instabilities in boiling microchannel systems, Int. J. Heat Mass Transf. 53 (2010) 2347–2360.
[49] M. Ozawa, S. Nakanishi, S. Ishigai, Y. Mizuta, H. Tarui, Flow instabilities in boiling channels: Part 1 Pressure drop oscillation, Bull. JSME 22 (1979) 1113–1118.
[50] J.E. Park, J.R. Thome, Critical heat flux in multi-microchannel copper elements with low pressure refrigerants, Int. J. Heat Mass Transf. 53 (2010) 110–122.
[51] W. Qu, I. Mudawar, Transport phenomena in two-phase micro-channel heat sinks, J. Electron. Packag. 126 (2004) 213–224.
[52] J.A. Boure, A.E. Bergles, L.S. Tong, Review of two-phase flow instability, Nucl. Eng. Des. 25 (1973) 165–192.
[53] S. Kakaç, B. Bon, A review of two-phase flow dynamic instabilities in tube boiling systems, Int. J. Heat Mass Transf. 51 (2008) 399–433.
[54] S.-M. Kim, I. Mudawar, Universal approach to predicting two-phase frictional pressure drop for mini/micro-channel saturated flow boiling, Int. J. Heat Mass Transf. 58 (2013) 718–734.
[55] S.-M. Kim, I. Mudawar, Review of databases and predictive methods for pressure drop in adiabatic, condensing, and boiling mini/micro-channel flows, Int. J. Heat Mass Transf. 77 (2014) 74–97.
[56] H.Y. Wu, P. Cheng, Visualization and measurements of periodic boiling in silicon microchannels, Int. J. Heat Mass Transf. 46 (2003) 2603–2614.
[57] H. Wu, P. Cheng, Boiling instability in parallel silicon microchannels at different heat flux, Int. J. Heat Mass Transf. 47 (2004) 3631–3641.
[58] S.M. Zivi, Estimation of steady-state steam void-fraction by means of the principle of minimum entropy production, J. Heat Transf. 86 (1964) 247–252.
[59] D.R. Harper, W.B. Brown, Mathematical equations for heat conduction in the fins of air cooled engines, NACA Rep. 158, National Advisory Committee on Aeronautics, Washington, DC, 1922.
[60] Th.E. Schmidt, Heat transfer calculations for extended surfaces, Refrig. Eng. 49 (1949) 351–357.
[61] C.C. Wang, Y.J. Chang, Y.C. Hsieh, Y.T. Lin, Sensible heat and friction characteristics of plate fin-and-tube heat exchangers having plate fins, Int. J. Refrig. 19 (1996) 223–230.
[62] N.H. Kim, B. Youn, R.L. Webb, Air-side heat transfer and friction correlations for plain fin-and-tube heat exchangers with staggered tube arrangements, J. Heat Transf. 121 (1999) 662–667.
[63] T.L. Bergman, F.P. Incropera, A.S. Lavine, D.P. DeWitt, Fundamentals of Seat and Mass Transfer, seventh ed., Wiley and Sons, New York, 2011.
[64] G. Rigot, Fluid capacity of an evaporator in direct expansion, Plomberie, No. 328, 133-144, 1973 (English Trans., ORNL-tr-5217, Oak Ridge National Laboratory, Oak Ridge, TN).
[65] F. Ahrens, Heat pump modeling, simulation and design, in: Proc. NATO Advanced Study Institute on Heat Pump Fundamentals, Espinho, Spain, 1980.
[66] J.R.S. Thom, Prediction of pressure drop during forced circulation boiling of water, Int. J. Heat Mass Transf. 7 (1964) 709–724.
[67] S.L. Smith, Void fractions in two-phase flow: a correlation based upon an equal velocity head model, Proc. Inst. Mech. Eng. 36 (1969) 647–664.

[68] R.W. Lockhart, R.C. Martinelli, Proposed correlation of data for isothermal two-phase, two-component flow in pipes, Chem. Eng. Prog. 45 (1949) 39–48.
[69] G.B. Wallis, One-dimensional two-phase flow, McGraw-Hill, 1969, pp. 51–54.
[70] P. Domanski, D. Didion, Computer modeling of the vapor compression cycle with constant flow area expansion device, NBS Build. Sci. Ser. 155 (1983).
[71] C.J. Baroczy, Correlation of liquid fraction in two-phase flow with application to liquid metals, Chem. Eng. Prog. Symp. Ser. 61 (1965) 179–191.
[72] A. Premoli, D. Francesco, A. Prina, An empirical correlation for evaluating two-phase mixture density under adiabatic conditions, in: European Two-Phase Flow Group Meeting, Milan, Italy, 1970.
[73] G.A. Hughmark, Holdup in gas-liquid flow, Chem. Eng. Prog. 58 (1962) 62–65.
[74] W.W. Akers, H.F. Rosson, Condensation inside a horizontal tube, Chem. Eng. Prog. Symp. 56 (1960) 145–149.
[75] A. Cavallini, R. Zecchin, A dimensionless correlation for heat transfer in forced convection condensation, in: Proc. Sixth Int. Heat Transfer Conf., vol. 3, Tokyo, Japan, 1974, pp. 309–313.
[76] M.M. Shah, A general correlation for heat transfer during film condensation inside pipes, Int. J. Heat Mass Transf. 22 (1979) 547–556.
[77] H. Haraguchi, S. Koyama, T. Fujii, Condensation of refrigerants HCFC 22, HFC 134a and HCFC 123 in a horizontal smooth tube (2nd report), Trans. JSME (B) 60 (1994) 245–252.
[78] M.K. Dobson, J.C. Chato, Condensation in smooth horizontal tubes, J. Heat Transf. 120 (1998) 193–213.
[79] K.W. Moser, R.L. Webb, B. Na, A new equivalent Reynolds number model for condensation in smooth tubes, J. Heat Transf. 120 (1998) 410–417.
[80] M.M. Shah, An improved and extended general correlation for heat transfer during condensation in plain tubes, HVAC&R Res. 15 (2009) 889–913.
[81] T. Bohdal, H. Charun, M. Sikora, Comparative investigations of the condensation of R134a and R404A refrigerants in pipe minichannels, Int. J. Heat Mass Transf. 54 (2011) 1963–1974.
[82] S.-M. Kim, I. Mudawar, Universal approach to predicting heat transfer coefficient for condensing mini/micro-channel flows, Int. J. Heat Mass Transf. 56 (2013) 238–250.
[83] A. Cavallini, G. Censi, D. Del Col, L. Doretti, G.A. Longo, L. Rossetto, C. Zilio, Condensation inside and outside smooth and enhanced tubes – a review of recent research, Int. J. Refrig. 26 (2003) 373–392.
[84] L. Friedel, Improved friction pressure drop correlations for horizontal and vertical two-phase pipe flow, in: European Two-Phase Flow Group Meeting, Ispra, Italy, Paper E2, 1979.
[85] H.J. Hickman, An asymptotic study of the Nusselt-Graetz problem, part I: large x behavior, J. Heat Transf. 96 (1974) 354–358.